Inflammation promotes tumor aggression by stimulating stromal cell-dependent collagen crosslinking and stromal stiffening

Ori Maller[1*], Allison P. Drain[1*], Alexander S. Barrett[2*], Signe Borgquist[3,4], Brian Ruffell[5], Pham T Thanh[2], Tina Gruosso[6], Hellen Kuasne[6], Johnathon N. Lakins[1], Irene Acerbi[1], J. Matthew Barnes[1], Travis Nemkov[2], Aastha Chauhan[7], Jessica Gruenberg[7], Aqsa Nasir[7], Olof Bjarnadottir[3], Zena Werb[8,9], Peter Kabos[10], E. Shelley Hwang[12], Morag Park[6], Lisa M. Coussens[5], Andrew C. Nelson[7], Kirk C. Hansen[2,14] and Valerie M. Weaver[9,13,14,15]

[1]Department of Surgery, Center for Bioengineering and Tissue Regeneration, University of California, San Francisco, California, USA
[2]Department of Biochemistry and Molecular Genetics, University of Colorado Denver - Anschutz Medical Campus, Aurora, CO, USA
[3]Division of Oncology and Pathology, Department of Clinical Sciences, Lund, Lund University
[4]Clinical Trial Unit, Clinical Studies Sweden, Forum South, Skåne University Hospital, Lund, Sweden
[5]Cell, Developmental & Cancer Biology, Oregon Health & Science University; Knight Cancer Institute, Oregon Health & Science University, Portland, Oregon, USA
[6]Goodman Cancer Research Centre, McGill University, Montreal, QC, Canada; Department of Biochemistry, McGill University, Montreal, QC, Canada; Department of Oncology, McGill University, Montreal, QC, Canada
[7]Department of Laboratory Medicine and Pathology, University of Minnesota, Minneapolis, MN, USA
[8]Department of Anatomy and Biomedical Sciences Program, University of California, San Francisco CA, USA
[9]UCSF Helen Diller Comprehensive Cancer Center, University of California, San Francisco, San Francisco, CA, USA
[10]Department of Medicine, Division of Medical Oncology, University of Colorado Anschutz Medical Campus, Aurora, Colorado, USA
[11]Department of Pathology, University of California, San Francisco, CA, USA
[12]Department of Surgery, Duke University Medical Center, Durham, NC, USA
[13]Departments of Bioengineering and Therapeutic Sciences, and Radiation Oncology, Eli and Edythe Broad Center of Regeneration Medicine and Stem Cell Research

[*]These authors contributed equally to this work
[14]These authors jointly supervised this work

The authors have no conflicts of interest to declare.

[15]**Corresponding Author:**

Valerie M. Weaver
Center for Bioengineering and Tissue Regeneration
Department of Surgery
University of California, San Francisco
Telephone: (415) 476-3826
Email: valerie.weaver@ucsf.edu

1   **Abstract**

2   Collagen deposition and stromal stiffening accompany malignancy, compromise treatment, and

3   promote tumor aggression. Clarifying the molecular nature of and the factors that regulate

4   extracellular matrix stiffening in tumors should identify biomarkers to stratify patients for therapy

5   and therapeutic interventions to improve outcome. We profiled lysyl hydroxylase- and lysyl

6   oxidase-mediated collagen crosslinks and quantified the greatest abundance of total and complex

7   collagen crosslinks in more aggressive human breast cancer subtypes with the stiffest stroma.

8   These tissues also harbored the highest number of tumor-associated macrophages (TAM), whose

9   therapeutic ablation not only reduced metastasis, but also concomitantly decreased accumulation

10   of collagen crosslinks and stromal stiffening. Epithelial-targeted expression of the crosslinking

11   enzyme lysyl oxidase had no impact on collagen crosslinking in PyMT mammary tumors, whereas

12   stromal cell targeting did. Consistently, stromal cells in microdissected human tumors expressed

13   the highest level of collagen crosslinking enzymes. Immunohistochemical analysis of a cohort of

14   breast cancer patient biopsies revealed that stromal expression of lysyl hydroxylase two, an

15   enzyme that induces hydroxylysine aldehyde-derived collagen crosslinks and stromal stiffening

16   correlated significantly disease specific mortality. The findings link tissue inflammation, stromal

17   cell-mediated collagen crosslinking and stiffening to tumor aggression and identify lysyl

18   hydroxylase two as a novel stromal biomarker.

19

20   **Significance**

21   We show infiltrating macrophages induce stromal fibroblast, and not epithelial, expression of

22   collagen crosslinking enzymes that drive tumor stiffening. Stromal enzyme LH2 is significantly

23   upregulated in breast cancer patients with the stiffest stroma, the most trivalent HLCCs and the

24   worst prognosis, underscoring its potential as a biomarker and therapeutic target.

25

26   **Introduction**

27   Pathological accumulation of extracellular matrix (ECM) accompanies the formation of all

28   solid tumors(1-3). The tumor ECM is composed primarily of interstitial collagen that is

29   progressively reorganized and stiffened(2,4). The collagenous fibrotic tumor ECM compromises

30   treatment and is linked to poor patient prognosis(5-8). Tumor biopsy analysis showed that a

31   thick fibrous collagenous ECM associates with less differentiated tumors and that this

32   phenotype predicts poor patient survival, emphasizing the relevance of collagen

33   architecture(1,4,9). Patients with pancreatic ductal adenocarcinomas (PDACs) that are

34   surrounded by stiff, thick fibrous collagens have a shorter survival, and invasive breast

35   carcinomas with the stiffest ECM stroma at their invasive front are the most aggressive(1,2).

36   These observations suggest that stromal stiffness reflects collagen organization may be an

37   important prognostic variable. Consistently, preclinical studies using organotypic cultures and

38   rodent models provide plausible evidence for a causal relationship between collagen

39   organization, stromal stiffness, tumor cell invasion in culture, and metastasis *in vivo*(10-14).

40   These findings underscore the clinical relevance of collagen architecture and stiffness to

41   malignancy, and emphasize the need to clarify the molecular nature of the collagenous ECM so

42   that new biomarkers can be identified and anti-cancer therapeutics may be

43   developed(1,2,15,16).

44   Interstitial type I fibrillar collagen is the ECM component that contributes most

45   significantly to the tensile strength of tissue(17). The tensile strength of interstitial collagen

46   depends upon the activities of two major families of enzymes: the lysyl hydroxylases (LH; gene

47   name procollagen-lysine, 2-oxoglutarate 5-dioxygenase or PLOD) and the lysyl oxidases (LOX),

48   which regulate fibrillogenesis of newly synthesized collagen molecules through intermolecular

49   covalent crosslinking(18-21). Fibrotic human tumors express high levels of LOX and LH

50   enzymes(22). Tumor grade and overall patient survival associate with total tissue LOX and

51   PLOD2 mRNA(21,23-25). Pharmacological or antibody-mediated inhibition of LOX in MMTV-

3

52   Her2/Neu mice or genetic reduction of PLOD2 in subcutaneously-injected lung tumor epithelial

53   cells reduce tissue fibrosis, stromal stiffening and collagen crosslinking and concomitantly

54   decrease tumor incidence and aggression(12,23). Moreover, elevating LOX or LH2-mediated

55   collagen crosslinking enhances fibrosis and stromal stiffness and promotes malignant

56   transformation and tumor aggression in lung and mammary xenografted tumors(12,23). These

57   observations suggest that the direct targeting of specific collagen crosslinking enzymes has

58   clinical merit for the treatment of cancer. However, given caveats with recent clinical trials

59   targeting ECM modifiers including suboptimal activity of inhibitory treatments and the risk of off-

60   target effects, strategies designed to interfere with the induction and activation of these

61   crosslinking enzymes offer an attractive alternative(26). Towards this goal, the identification and

62   causal implication of additional factors that regulate the levels and/or activity of collagen

63   crosslinking enzymes has the potential to identify new predictive biomarkers and alternative

64   anti-tumor treatment targets.

65   Pre-neoplastic lesions are inflamed, and pathological fibrosis correlates with

66   inflammation(27,28). Chronic inflammation and experimental manipulations that promote

67   inflammation in rodent models induce fibrosis by secreting factors such as metalloproteinases

68   and TGFβ(14,28-31). Furthermore, fibrotic tumors are frequently inflamed, and this inflammation

69   promotes tumor aggression, whereas either inhibiting inflammation or decreasing macrophage

70   infiltration reduce tumor metastasis and enhance anti-tumor treatment(2,27,32-35).

71   Nevertheless, it remains unclear if inflammation promotes tumor progression and aggression by

72   inducing stromal stiffening, and if so, whether this is regulated via epithelial and/or stromal

73   fibroblast-mediated collagen remodeling and crosslinking.

74   **Results**

75   **xAAA profiling identifies increased levels of collagen crosslinks and stromal stiffness as**

76   **indicators of breast tumor aggression**

4

77   To clarify the role of collagen crosslinking in tumor fibrosis we developed a crosslinked

78   amino acid analysis (xAAA) method that enabled the characterization and quantification of

79   specific collagen crosslinks in tissues across a wide range of collagen levels. We utilized solid

80   phase extraction (SPE) enrichment followed by high pH amide hydrophilic chromatography

81   (HILIC) coupled to a benchtop orbitrap (QExactive) mass spectrometer for these

82   measurements. The validated method detected all known LOX-generated crosslinks including

83   divalent (lysinonorleucine, dihydroxy lysinonorleucine), trivalent (pyridinoline and deoxy-

84   pyridinoline) and tetravalent (desmosine and isodesmosine) crosslinked amino acids linearly

85   over four orders of magnitude, with calculated limits of quantification (LLOQ) in the femtomolar

86   range (**Suppl. Fig. 1; Suppl. Table 1**)(36). The technique revealed a positive correlation

87   between collagen crosslinking and abundance in excised human clinical specimens with very

88   low to very high collagen concentrations and varying mechanical properties (**Suppl. Fig 2**). The

89   method also identified a subset of hydroxylysine aldehyde (Hyl^{ald})-derived collagen crosslinks

90   (HLCCs) crucial for the mechanical strength of tissue(17,37).

91   We next obtained snap-frozen biospecimens of normal human breast tissue (N=10; age

92   between 22 and 58) and human tumor biopsies representing early stage (stage 1-2) invasive

93   breast cancers (IBC) excised from mastectomy specimens. Molecular subtyping that subdivides

94   human breast tumors stratified by estrogen receptor (ER+) and human epidermal growth factor

95   receptor two (HER2+) status and ER/PR/HER2-negative (triple negative; TN) is a key

96   determinant used to direct the treatment of breast cancer patients. Accordingly, we chose

97   human breast tumor biopsies that represented ER+ (N=8; age between 42 and 71); HER2+

98   (N=6; age between 40 and 76) and TN (N=6; age between 50 and 71). H&E stained tissue

99   sections confirmed the presence of normal glandular structures in the normal controls and

100   invasive breast cancer in the tumor specimens (**Fig. 1a; top panels**). Polarized light imaging of

101   Picrosirius-stained (PS) tissue revealed that the normal breast tissue stroma had very little

102   fibrillar collagen, whereas stromal tissue in all patients with IBCs contained abundant fibrillar

5

103   collagen (**Fig. 1a; middle panels)** that second harmonic generation (SHG) imaging indicated

104   was thicker and more linearized (**Fig. 1a; bottom panels**). Polarized light microscopy and two-

105   photon imaging further revealed that the level of fibrosis in the tissue was higher in HER2+ as

106   compared to the ER+ breast tumors, and was further increased in the TN tumors, consistent

107   with our previous report that TN tumors contain a high density of aligned collagen fibers (**Fig.**

108   **1a; middle** and **bottom panels**)(2). AFM microindentation revealed a significant increase in the

109   elastic modulus of the stroma associated with the invasive front of all the IBC tissues (**Fig.**

110   **1b**)(2,4,12). xAAA analysis revealed a significant increase in total collagen crosslinking in all the

111   IBCs (**Fig. 1c, Suppl. Fig. 5**). These findings are consistent with an association between

112   collagen crosslinks, tissue fibrosis and stromal stiffness, as has been previously documented in

113   experimental murine models of mammary cancer(12). Interestingly, when we subdivided the

114   IBC collagen crosslinking analysis into breast tumor subtype the most significant increase in

115   total collagen crosslinks was calculated to be in the TN breast tumors (**Fig. 1i**). Furthermore,

116   biochemical quantification of total tissue collagen 1A1 or 1A2 did not account for the higher total

117   number of collagen crosslinks in the TN breast tumor tissue (**Fig. 1k**). Instead, molecular

118   characterization of the isolated tissue collagen revealed that the TN tumors had a distinctive

119   crosslink profile due to a strong preference for a combination of DHLNL, Pyr, and d-Pyr

120   crosslinks (**Fig. 1d-j**). Subtype analysis further revealed that the level of hydroxylysine

121   aldehyde-derived collagen crosslinks (HLCCs) in the TN subtype correlated significantly and

122   positively with the stiffness of the stroma at the invasive front of the tumor tissue (**Fig. 1l**). These

123   findings highlight the importance of HLCC collagen crosslinking in breast cancer aggression.

124   **Increased collagen crosslinking correlates with high expression of stromal LOX and**

125   **PLOD2 in aggressive tumor subtypes**

126   To determine if the observed increase in collagen crosslinking and stromal stiffness in

127   TN tumors was related to the expression levels of enzymes implicated in regulating collagen

128   crosslinking, we analyzed publicly available human breast cancer gene expression array data (n

129   = 1904) for the genes coding these enzymes and examined their correlation to breast cancer

130   subtype. Bioinformatics analyses revealed a significant increase in the major collagen

131   crosslinking enzyme LOX, but not lysyl oxidase like two (LOXL2), in the more aggressive HER2

132   and TN tumor subtypes and indicated that LOX levels were particularly high in TN tumors (**Fig.**

133   **2a-b**). The arrays also showed bulk gene expression of PLOD2, the major regulator of HLCC

134   accumulation, to be highly upregulated in aggressive human TN breast cancers (**Fig. 2c**).

135   To gain insight into the cellular sources of LOX and LH2 in human tumors, we used laser

136   capture microdissection to isolate regions of tumor epithelium and stroma to identify the origins

137   of LOX and LH2 in invasive human breast cancers (38,39). Gene expression analysis of stromal

138   and epithelial compartments revealed that the stromal cells in the tumor tissue expressed

139   significantly more LOX and PLOD2 than the associated tumor epithelium. The data further

140   indicated that this relationship was more evident in the breast tissue from women with ER-/PR-

141   breast cancer that is frequently the more aggressive tumor subclass (**Fig. 2d-g**).

142   The findings implicate, but do not definitively demonstrate a role for LOX and PLOD2 in

143   generating the increased level and greater complexity of collagen crosslinking we quantified in

144   the more aggressive human breast tumors. Nevertheless, the combination of these gene

145   expression data with our findings showing increased collagen crosslink abundance provide

146   compelling evidence to suggest that increased expression of LOX and PLOD2, particularly from

147   stromal cells, likely contribute to elevated levels of collagen crosslinks and HLCCs in TN tumors.

148   Moreover, given that TN tumors are the most aggressive and lethal breast cancer, these data

149   link human breast tumor aggression to increased levels of total and complex collagen crosslinks

150   and higher stromal stiffness. Accordingly, the findings implicate the collagen crosslinking

151   enzymes LOX and LH2, and by extension factors that regulate their expression, in breast

152   cancer aggression.

153   **Stromal — and not epithelial — crosslinking enzymes regulate tissue fibrosis and**

154   **collagen crosslinking *in vivo***

155   Prior studies demonstrated that both cancer cell lines and stromal fibroblasts express

156   LOX and LH2 to induce tissue stiffening and fibrosis implying they also drove collagen cross-

157   linking. Seminal articles identified hypoxia-induced HIF1a as a key regulator of tumor epithelial

158   LOX and LH2 expression and suggested epithelial secretion of these enzymes drives collagen

159   remodeling, crosslinking and stiffening that foster tumor cell dissemination and primes the pre-

160   metastatic niche to facilitate metastatic colonization (22,24,25). Our analysis of breast cancer

161   clinical specimens showed that the stromal cells in the breast tissue express higher levels of

162   LOX and PLOD2 as compared to the breast tumor epithelium. Moreover, our prior studies

163   showed LOX is expressed in stromal fibroblasts in a transgenic mouse model of ErbB2-induced

164   mammary tumor malignancy. Furthermore, we demonstrated that fibroblasts expressing LOX

165   injected into a cleared mammary fat pad not only induced ECM remodeling and stiffening but

166   also potentiated the growth and malignant progression of pre-malignant tumor cells injected into

167   the modified glands (12). Thus, the relative contribution of tumor- and stromal- derived collagen

168   crosslinking enzymes to tumor fibrosis, ECM remodeling and collagen crosslinking remains

169   unclear; particularly in the context of spontaneous tumors and patient tumors in which the ECM

170   evolves concurrently with tumor progression.

171   To directly test the extent to which epithelial-derived LOX can crosslink collagen and

172   induce tissue fibrosis and stromal stiffening in mammary tissue, we created a genetically

173   engineered mouse model (GEMM) in which we targeted and controlled luminal epithelial-

174   specific expression of mouse LOX using the MMTV-rtTA promoter (Epithelial LOX

175   overexpression [OX]). (**Fig. 3a, Suppl. Fig. 6a-b**). We crossed these mice into the PyMT

176   spontaneous mammary tumor model to enhanced LOX expression in the mammary tumor

177   epithelium (PyMT epithelial LOX OX) and assayed their stromal phenotype as compared to the

178   mammary glands from age-matched PyMT control mice (PyMT). Again, despite confirming

179   ectopic LOX expression and elevated levels of cleaved LOX protein in the mammary tumor

180   epithelial compartment (**Suppl. Fig 6c**), we were not able to detect any increase in the levels,

8

181   nor any altered organization of the mammary gland interstitial collagen (**Fig 3b-c**). Moreover,

182   xAAA crosslinking analysis revealed that the level of collagen crosslinks between the PyMT

183   control and PyMT epithelial LOX OX mammary gland stroma were indistinguishable (**Fig. 3d-i**).

184   Nevertheless and importantly, we could easily and consistently detect a significant increase in

185   fibrillar collagens, collagen crosslinks and stromal stiffness in the PyMT mammary tumors as

186   compared to age-matched FVB mammary glands lacking tumors (**Fig. 4c,f-k**). These studies

187   both validate the sensitivity of our crosslinking assay and imply that tumor epithelial LOX is not

188   the primary driver of collagen crosslinking and stiffening in endogenous mammary tumors.

189   We and others have implicated stromal fibroblast LOX as a key promoter of epithelial

190   tumor progression and aggression(12,14,40). To directly test the functionality of the ectopically-

191   expressed LOX and the relevance of fibroblast-specific expression of LOX, we next created

192   mouse cohorts of PyMT GEMMs in which we restricted ectopic LOX expression to the stromal

193   population using the Col1a1-tTA promoter (MMTV-PyMT+/-; Col1a1-tTA+/-;TetO_mLox+/-;

194   herein denoted PyMT LOX OX) (**Fig. 4a, Suppl. Fig. 7b**). To begin with, induction of LOX in the

195   stromal cells markedly enhanced the amount of fibrillar collagen in the MMTV-PyMT LOX OX

196   mammary glands, as revealed by quantification of polarized images of Picrosirius Red stained

197   tissue (**Fig. 4b, second row images; quantified in c**). We also detected more and thicker

198   linearized interstitial collagen when LOX was increased in the stromal cells by two-photon

199   second harmonic generation imaging (**Fig. 4b, third row panels**). In addition, immunostaining

200   revealed more phosphorylated tyrosine 397 focal adhesion kinase protein (^{pY397}FAK) in the

201   mammary epithelium of the glands in which stromal LOX was elevated (**Fig. 4b, bottom**

202   **panels**), likely reflecting the increase in elasticity that we measured in the tissue stroma using

203   atomic force microscopy (AFM) indentation(12) (**Fig. 4d-e & Suppl. Fig. 9b**). Consistently, we

204   measured higher levels of total collagen crosslinks in the PyMT LOX OX mice as compared to

205   the levels quantified in the MMTV-PyMT control glands (**Fig. 4f**). Furthermore, the most

206   significant increases that we quantified in the PyMT LOX OX glands were dihydroxy

9

207   lysinonorleucine (DHLNL) and pyridinoline (Pyr) crosslinks (**Fig. 4g-k**), which are the crosslinks

208   generated through the HLCC pathway that promote mechanical stability and strength in skeletal

209   tissue(37,41). Of note, we did not detect any increase in DHLNL or Pyr in the mammary glands

210   in which ectopic LOX expression was elevated in the mammary epithelium using the MMTV

211   promoter (**Fig. 3g-h**). These findings imply that stromal cells are the primary regulators of

212   interstitial collagen crosslinking and stromal stiffening in mammary tumors.

213   **Tissue inflammation regulates tissue fibrosis, collagen crosslinking and stromal**

214   **stiffening**

215   Cancer progression is accompanied by tissue inflammation and the most aggressive

216   human breast tumors with the stiffest invasive stroma harbor the highest number of

217   macrophages(2,35). Consistently, decreasing the number of tumor macrophages, either through

218   genetic ablation of macrophage colony stimulating factor (CSF-1) or via pharmacological and

219   inhibitory antibody treatment with anti-CSF1 antibody, reduces lung metastasis in the PyMT

220   mouse model of mammary cancer(33,34,42,43). Interestingly, macrophage ablation was more

221   effective at preventing lung metastasis in the PyMT mammary tumor model when the treatment

222   was initiated early, prior to malignant transformation and coincident with the onset of tissue

223   fibrosis(33). These findings raise the intriguing possibility that macrophage ablation may

224   regulate tumor aggression, at least in part, by promoting collagen remodeling and inducing ECM

225   crosslinking and stromal stiffening (**Fig. 3 & 4**).

226   To assess the possibility that there is a causal association between macrophage-

227   mediated tissue inflammation, tumor fibrosis and ECM stiffening and mammary tumor

228   aggression, PyMT mice were treated with anti-CSF-1 antibody or a non-specific IgG control

229   antibody commencing at four weeks of age, prior to the onset of ductal hyperplasia(44). Mouse

230   cohorts (6/treatment group/time point) were sacrificed at eight and eleven weeks of age.

231   Immunostaining confirmed efficient reduction of mammary tumor tissue macrophages at eight

232   weeks of age, as evidenced by significantly reduced F4-80 immunostaining that was also

10

233   evident in the eleven week old treated tissue (**Fig. 5a top panel, Suppl. Fig. 8a**). The excised

234   lungs from the eleven week mice confirmed reduced frequency of lung metastasis in the anti-

235   CSF-1 antibody-treated group (**Fig. 5b**), consistent with our prior work documenting a significant

236   inhibition of lung metastasis in fourteen week old mice when anti-CSF-1 treatment was initiated

237   at four weeks(33). The mammary glands from the eight and eleven week old mice were excised

238   and analyzed for fibrosis and biomechanical properties (**Fig. 5a,c-i**). Despite confirming an

239   equivalent number of fibroblasts in the treated and nontreated groups, polarized images of PS

240   stained tissue revealed lower levels of total fibrillar collagen in the stroma of the eight week anti-

241   CSF1 antibody treated group (**Fig. 5a, third row panel, Suppl. Fig. 10b-c**). AFM

242   microindentation additionally demonstrated that the tissue stroma from both the eight week old

243   (**Fig. 5d**), and the eleven week old (not shown) mammary glands was softer, likely accounting

244   for the reduced integrin mechanosignaling detected in the CSF1-antibody treated tissue, as

245   revealed by less intense staining for ^{pY397}FAK **(Fig. 5a, second row panel)**. Consistently, we

246   also observed reduced levels of Lox mRNA in eight week, anti-CSF1 treated mice by in situ

247   hybridization (**Fig. 5a, bottom panel, Fig. 5e**). In agreement with prior studies, nearly all the

248   detected Lox mRNA was restricted to stromal cells (**Fig 5a, bottom panel**)(14). These findings

249   suggest that reducing the level of tumor-associated macrophages (TAMs) not only prevents

250   lung metastasis but also concomitantly reduces tissue fibrosis and stiffening, likely by

251   preventing stromal cell activation.

252   TAMs secrete abundant TGFβ that stimulates fibroblast differentiation to a myofibroblast

253   phenotype and induces expression of collagen crosslinking enzymes including LOX(14). PCR

254   analysis of flow activated cell sorted (FACS) cells from the transformed mammary glands of

255   PyMT mice (11 weeks) confirmed that the TAMs expressed by far the highest levels of TGFβ,

256   as compared to neoplastic epithelium and the cancer-associated fibroblasts (**Fig. 5j**). These

257   findings suggest that the tumor infiltrating macrophages could promote fibrosis and stromal

258   stiffening through secreted TGFβ; a finding supported by a strong stromal pSMAD2 (SMAD2

259   pS465/467) in the IgG control antibody-treated PyMT mammary glands (**Fig. 5k-l**). To examine

260   whether TAM recruitment could regulate collagen crosslinking in human tumors we queried a

261   publicly available human breast tumor gene expression data set for TAM markers and collagen

262   modifying enzymes. Consistent with a role for TAMs in stimulating expression of collagen

263   modifying enzymes, gene expression of the TAM marker CD163 positively correlated with both

264   LOX and PLOD2 but not LOXL2 in human breast tumors (n = 1904) (**Fig. 5m-o**). Moreover, co-

265   staining of resected human breast tumors with the macrophage/monocyte marker CD68 and the

266   downstream TGFβ signaling molecule pSMAD2 Ser465/467 revealed a significant positive

267   correlation between pSMAD2 Ser465/467 and infiltrating tumor macrophages at the invasive

268   front of human breast tumors (**Fig. 5p-q**). Furthermore, FACS analysis established a significant

269   correlation between the infiltrating tumor associated macrophages, as demonstrated by

270   CD14^{hi}CD11b$^+$ HLA-DR$^+$ cell surface markers normalized to total CD45 infiltrating cells, and the

271   elastic modulus of the invasive front of human invasive breast cancers (**Fig. 5r**). These findings

272   suggest that tumor inflammation and macrophage secreted factors such as TGFβ could

273   promote tissue fibrosis by enhancing fibroblast expression of the collagen crosslinking enzymes

274   LOX and PLOD2, but not LOXL2, to induce collagen crosslinking and stromal stiffening.

275   **LH2 inhibition reduces lung metastasis and stromal LH2 predicts poor prognosis in**

276   **breast cancer patients**

277   Using the data set generated from the micro-dissected tumors, we next explored the clinical

278   relevance of epithelial vs. stromal LOX and PLOD2 expression by assessing their relative

279   contribution to overall survival in breast cancer patients. Surprisingly, neither stromal cell nor

280   epithelial LOX predicted overall patient survival in this cohort (**Fig. 6a-b**). However, the findings

281   clearly showed that overexpression of stromal PLOD2, but not epithelial PLOD2, significantly

282   correlated with poor breast cancer patient prognosis (**Fig. 6c-d**). The data provide further

283   evidence that HLCCs, formed primarily through the activities of collagen crosslinking enzymes

284   expressed by stromal cells, promote breast tumor aggression that contributes to poorer overall

285   survival. The findings also highlight the importance of the collagen crosslinking profile and its

286   potential impact on stromal stiffness in tumor aggression.

287   LH2 (the protein encoded by PLOD2) is a key enzyme that regulates the level of HLCC

288   crosslinking of fibrillar collagen and consequently contributes substantially to the tensile

289   properties of the tissue stroma(19,23,45). We quantified the highest level of HLCC crosslinking

290   and the stiffest invasive front in the breast tissue from women with the most aggressive breast

291   cancers (**Fig. 1j**). Consistently, when we analyzed the gene expression data from a published

292   cohort of breast cancer patients we observed that ER-/HER2- (TN; n=133) breast cancers

293   express the highest level of the PLOD2 gene transcript as compared to the levels expressed in

294   HER2+ (n=73) and ER+/HER2- (luminal, n=314) breast tumors (**Suppl. Fig. 11a**)(46). Further

295   analysis showed that high PLOD2 expression in breast cancer patients with HER2+ and TN

296   tumors significantly predicts reduced distant metastasis-free survival (DMFS), as well as

297   increased risk of relapse in TN tumors (**Suppl. Fig. 11b-d**)(46,47). These findings implicate

298   PLOD2/LH2 as a key regulator of breast tumor aggression through its ability to induce the

299   HLCC crosslinking of fibrillar collagens that enhance the stiffness of the tumor stroma.

300   To evaluate whether LH2 does enhance stromal stiffness to promote breast tumor

301   aggression, we systemically treated a cohort of PyMT mice with the LH2 inhibitor minoxidil or

302   vehicle (PBS) from five weeks of age until sacrifice at either 11-12 weeks or 13-14 weeks of age

303   (**Fig. 6e**). Consistent with its predicted role in enhancing stromal stiffness through modifying the

304   nature of collagen crosslinks, AFM microindentation revealed that the phenotypically-similar

305   collagen-rich ECM adjacent to tumors from the minoxidil treated mice (see polarized imaging of

306   picrosirius red stained tissue) was significantly softer when compared to the vehicle-treated

307   age/stage-matched PyMT mice (**Fig. 6f-h**). Furthermore, inhibiting LH2 also significantly

308   decreased lung metastasis, causally linking HLCC collagen crosslinking to stiffness-mediated

13

309   breast tumor aggression (**Fig. 6i**). Our gene expression data from the epithelial and stromal

310   microdissection cohort indicated that stromal PLOD2, but not epithelial PLOD2, strongly

311   predicted poor survival in breast cancer patients. Therefore, we next sought to definitively

312   assess the relative contribution of stromal versus neoplastic epithelial LH2 protein expression to

313   human breast tumor aggression using a large tissue array of annotated human breast tumor

314   biopsies. To accomplish this, we first developed an LH2 immunostaining protocol (IHC) and

315   then we analyzed neoplastic epithelial and stromal expression of the LH2 enzyme in tissue

316   biopsies from a large cohort of histopathologically classified breast cancer patients (N=505) with

317   accompanying clinical information and follow up data (**Suppl. Table 2** and **Suppl. Table 3**). LH2

318   IHC staining in the epithelium and stromal cells was scored as low, intermediate and high and

319   the relationship between epithelial versus stromal expression and breast cancer patient

320   outcome was calculated (**Fig. 6j; Suppl Fig. 12a**). IHC scoring analysis revealed that only a

321   modest number of patients with poorly differentiated breast tumors expressed moderate to high

322   levels of epithelial LH2 (**Suppl. Fig. 12b**); a finding that accords with prior links between tumor

323   size, hypoxia and LH2-dependent tumor aggression(23,24). More strikingly however, we

324   observed that a disproportionately high number of breast cancer patients with moderately and

325   poorly differentiated breast tumors had high stromal cell LH2 (indicated by an H score of above

326   230; **Fig. 6k**). These data and our observation that even well differentiated breast tumors

327   express intermediate levels of stromal cell LH2 (H score above 120 and equal or less than 230)

328   imply that stromal cell LH2, rather than epithelial LH2, may be a more robust indicator of breast

329   tumor aggression. Consistently, stratification of breast tumor patient analysis into ER+/HER2-

330   (N=296); HER2+ (N=36) and TN (N=32) showed an enrichment for intermediate and high

331   stromal LH2 H-score in the more aggressive cancer subtypes (**Suppl. Table 2** and **Suppl.**

332   **Table 3**). Furthermore, we uncovered a significant correlation between high stromal cell LH2 H-

333   score and shorter breast cancer patient-specific survival when adjusted for age at diagnosis

334   (**Fig. 6l**). We also established a significant association between stromal cell but not epithelial

14

335   LH2 levels and survival in lymph node positive breast cancer patients but not lymph node

336   negative breast cancers (**Fig. 6m-n; Suppl Fig. 12d-e**). These clinical data identify stromal cell

337   LH2 as a novel biomarker with potential to predict metastatic disease and poor patient survival

338   among breast cancers overall, as well as within the highest risk TN breast cancer subtype.

339

340   **Discussion:**

341   We identified infiltrating macrophages as key regulators of stromal cell-mediated

342   collagen crosslinking, stromal stiffening and tumor metastasis. Our clinical findings corroborated

343   our experimental results, revealing significant associations between macrophages and collagen

344   crosslinking enzymes providing evidence for a critical impact of inflammatory stromal cell-

345   mediated collagen crosslinking and stromal stiffening in tumor aggression and patient outcome.

346   Diverse subsets of myeloid cells account for adverse patient outcomes because they

347   differentially promote angiogenesis, tumor cell intravasation, and suppress the anti-tumor

348   immune response(48). Our results expand this perspective to include a key role for early

349   infiltrating macrophages in initiating a collagen crosslinking and stiffening program that

350   ultimately fosters tumor aggression and progression. We also determined that TN breast

351   cancers contain much higher amounts of LH2- and LOX-derived collagen crosslinks.

352   Specifically, we demonstrated that significantly higher levels of HLCC crosslinks could explain

353   their higher stromal stiffness and aggressiveness(2). Intriguingly, in depth collagen analysis

354   suggested that each breast tumor subtype exhibits a distinct collagen organization, stiffness and

355   crosslinking profile, raising the possibility that distinct collagen architectures and crosslinking

356   signatures may reflect differences in tissue pathobiology. Indeed, TN breast cancers often

357   present with high macrophage infiltration; an observation that is consistent with our AFM, two

358   photon and collagen crosslinking analysis data(2). Given that the immune cell infiltrate

359   significantly influences treatment response it is tempting to speculate that distinct collagen

360   architectures, crosslinking signatures and stiffnesses similarly regulate therapeutic efficacy.

15

361   We determined that stromal LH2 is a robust predictor of survival in breast cancer

362   patients, especially in those that are lymph node positive, supporting a potentially important

363   clinical link to stromal collagen crosslinking. Our data also revealed that both the upregulation of

364   crosslinking enzymes and in turn, collagen crosslinking, occur at an early stage of malignancy

365   that is concurrent with tumor cell invasion and coincident with the accumulation of infiltrating

366   macrophages(49). In part, this may explain why therapeutics targeting LOX and LOXL2 have

367   thus far failed to significantly prolong cancer patient survival. Substantial levels of collagen

368   crosslinking are likely to have occurred prior to therapy administration, and while these agents

369   may prevent further crosslinking activity, they are not capable of reversing crosslinks or collagen

370   modifications already present in the tissue. The early initiation of collagen crosslinking also

371   suggests that a detectable increase in stromal LH2 may provide an early prognostic marker of

372   disease progression and aggression that could inform treatment strategies. To that end, our

373   results show for the first time that LH2-derived collagen crosslinks are not only a distinct feature

374   of enhanced stromal stiffening in TN breast cancer but are able to predict distant metastasis-

375   free survival. These results also suggest that the profile of collagen crosslinks, and not simply

376   crosslink abundance alone, may play a role in promoting tumor aggression, thus warranting

377   further investigations into the contributions of HLCCs to ECM mechanical properties and tumor

378   aggression.

379   Our findings identify fibroblasts as the dominant cell population that promotes

380   reorganization and crosslinking of interstitial collagen to stiffen the tissue stroma. Only stromal-

381   targeted, and not epithelial-targeted, tissue-specific inducible LOX produced any measurable

382   change in collagen architecture, stiffness or crosslink abundance in a spontaneous tumor

383   (25,50,51). Our conclusion is consistent with earlier work in which we failed to detect any

384   alterations in fibrosis, collagen organization or stiffness when LOXL2 was either genetically-

385   ablated, or ectopically-increased in the mammary epithelium of PyMT mouse tumors, despite

386   documenting a significant impact on metastasis(40). Nevertheless, it is possible that our bulk

387   assay would not detect any small increase in collagen crosslinking induced by invading tumor

388   cells expressing high levels of LOX. To this end, immortalized tumor cells engineered to

389   overexpress LOXL2 injected orthotopically as a bolus of cells were able to induce fibrosis and

390   quantifiable changes in collagen remodeling and tissue stiffening; a finding we too confirmed

391   using isolated PyMT tumor cells overexpressing the LOXL2 enzyme(40). Nevertheless, our data

392   support the notion that in spontaneous tumors, the proximity of stromal cells to collagen and

393   their significantly higher expression of crosslinking enzymes dictate the profile and extent of

394   collagen crosslinking. Given that LH2 modifies collagen intracellularly and stromal cells secrete

395   the vast majority of the interstitial fibrillar collagen, it is not surprising that this is the case(52,53).

396   Moreover, our results stress the necessity of choosing an appropriate model to study tumor

397   associated ECM remodeling and suggest that orthotopic models may fail to accurately

398   recapitulate the natural evolution of ECM in tumor progression.

399   Our findings not only underscore the importance of stromal stiffness and collagen

400   crosslinking in cancer-associated fibrosis and disease aggression, but also define in more detail

401   the molecular nature of collagen modifications that accompany pathological fibrosis. Clarifying

402   the nature of collagen modifications and specific mechanisms regulating those alterations in

403   fibrosis will assist in the strategic design of novel, efficacious strategies to combat progressive

404   fibrosis and should prove instrumental in enabling further experimentation to understand

405   pathological fibrosis. Indeed, defining the molecular regulators that stimulate collagen cross-

406   linking, and mechanisms that distinguish resolvable from non-resolvable fibrosis would identify

407   attractive therapeutic targets for several pathological fibrotic diseases with limited treatment

408   options.

409   **Methods:**

410   **Human breast specimen acquisition and processing**

411   Fresh human breast specimens from breast reduction, prophylaxis, or breast tumor mastectomy

412   were either embedded in an optimum cutting temperature (OCT) aqueous embedding

17

413   compound (Tissue-Plus, Scigen, Cat# 4583) within a disposable plastic base mold (Fisher, Cat#

414   22-363-554) and were snap frozen by direct immersion into liquid nitrogen and kept at -80°C

415   freezer until cryo-sectioning for analysis, or specimens were formalin fixed and paraffin

416   embedded (FFPE). All human breast specimens were collected from prospective patients

417   undergoing surgical resection at UCSF or Duke University Medical Center between 2010 and

418   2014. The selected specimens were de-identified, stored, and analyzed according to the

419   procedures described in Institutional Review Board (IRB) Protocol #10-03832 and #10-05046,

420   approved by the UCSF Committee of Human Resources and the Duke's IRB (Pro00034242)(2).

421   **Mouse studies**

422   Macrophages were depleted in MMTV-PyMT mice by i.p. injections of 1mg of anti-CSF1

423   antibody clone 5A1 or an IgG1 control every 7 days starting at 4 weeks of age. Mice were

424   sacrificed at 8 and 11 weeks of age for tissue analysis.

425   Minoxidil and PBS vehicle was administered by i.p. injections of 3 mg/kg minoxidil in PBS three

426   times per week starting at 6 weeks of age. Mice were sacrificed at 11-12 and 13-14 weeks of

427   age for tissue analysis.

428   **Generation of mice**

429   All mouse studies were maintained under pathogen-free conditions and performed in

430   accordance with the Institutional Animal Care and Use Committee and the Laboratory Animal

431   Research Center at the University of California, San Francisco.

432   **TetO-mLOX-eGFP construct and transgenic mouse generation**

433   Full length mouse Lox (mLox) cDNA was purchased from OriGene. The full length ORF was

434   amplified by PCR using forward and reverse primers respectively:

435   GCAGGGATCCGCCACCATGCGTTTCGCCTGGGCTG and

436   GGCGTCTAGAGCACCATGCGTTTCGCCTGGGCTGTGC. Following digestion with BamHI

437   and XbaI, the PCR product was inserted into pSK TetO IRES 3xnlsEGFP(54) downstream of

438   the Tet regulated minimal CMV promoter and a 5' UTR containing a chimeric intron of human β-

439   globin and immunoglobulin heavy chain genes, which was expressed as a bicistronic mRNA via

440   an internal ribosome entry site (IRES2) with eGFP targeted to the nucleus by a N terminal in

441   frame fusion of 3 tandem repeats of the SV40 nuclear localization sequence (nls). The fragment

442   containing the expression cassette from Tet regulated promoter to SV40 polyadenylation signal

443   (SV40pA) was agarose gel purified from XhoI– EagI digested donor plasmid and was used to

444   generate TetO-mLox-eGFP transgenic mice by pronuclear injection into FVB/n oocyte (Mouse

445   Biology Program at UC Davis; project number MBP-834; colony number PN663).

446   **Generation of MMTV-PyMT/Col1a1(2.3)-tTA/TetO-mLox-eGFP mice**

447   The MMTV-PyMT/Col1a1(2.3)-tTA/TetO-Rs1 triple transgenic mice were generated by

448   heterozygote or homozygote crosses of mice carrying the TetO-mLox-eGFP transgene with

449   mice carrying heterozygote of the Col1a1(2.3)-tTA transgene (line 139)(55) or MMTV-rtTA and

450   MMTV-PyMT transgene(56) to generate the experimental triple-transgenic genotype. In all

451   breeding thereafter, MMTV-PyMT/Col11a1-tTA or MMTV-rtTA/TetO-mLox-eGFP male mice

452   were crossed with TetO-mLox-eGFP female mice. Two mg/mL doxycycline hyclate (Alfa Aesar;

453   Cat# J60579) was added to 5% sucrose water to modulate TetO-mLox-eGFP transgene

454   expression.

455   **Preparation of human breast specimens for hydrolysis**

456   OCT was removed from tissue blocks by first transferring biospecimens to a conical tube and

457   then performing 5X washes with 70% ethanol followed by 5X washes with 18 MΩ H_2O[48]. Each

458   wash consisted of vortexing the sample for 15 minutes at 4°C and then centrifuging at 18,000 x

459   g for 15 minutes at 4°C. Between 1 and 3 milligrams of tissue was washed with 1X PBS buffer

460   by vortexing for 15 minutes at 4°C and then sonicated on ice for 20 seconds using a Sonic

461   Dismembrator M100 (ThermoFisher, San Jose, CA, USA). The homogenate was then

462   centrifuged at 18,000 x g for 20 minutes at 4°C. The supernatant was removed and the pellet

463   was re-suspended in 1mg/mL $NaBH_4$ (prepared in 0.1N NaOH) in 1X PBS for 1 hour at 4°C with

464   vortexing. The reaction was neutralized by adding glacial acetic acid to a final concentration of

465   0.1% (pH ~ 3 -4)(57). The sample was then centrifuged at 18,000 x g for 20 minutes at 4°C. The

466   supernatant was removed and the pellet was washed three times with 18 MΩ H_2O to remove

467   residual salt that could interfere with downstream LC-MS/MS analysis. The remaining pellet was

468   dried under vacuum for further analysis.

469   **Protein hydrolysis**

470   The dried sample was placed in a glass hydrolysis vessel and hydrolyzed in 6N HCl, 0.1%

471   phenol. The hydrolysis vessel is flushed with N2 gas, sealed and placed in a 110°C oven for 24

472   hours. After hydrolysis, the sample was cooled to room temperature and then placed at -80°C

473   for 30 minutes prior to lyophilization. The dried sample was re-hydrated in 100µL of 18 MΩ H_2O

474   for 5 minutes, then 100 µL of glacial acetic acid for 5 minutes and finally 400 µL of butan-1-ol for

475   5 minutes. Importantly, 10 µL of sample is removed after re-hydration in water and saved for

476   determination of hydroxyproline content.

477   **Preparation of crosslink enrichment column**

478   CF-11 cellulose powder is loaded in a slurry of butan-1-ol: glacial acetic acid, water (4:1:1)

479   solution onto a Nanosep MF GHP 0.45µm spin columns until a settled resin bed volume of

480   approximately 5mm is achieved. The resin is washed with 1.5 mL 4:1:1 organic mixture using an

481   in-house vacuum manifold set up. Re-hydrated samples are then loaded onto individual

482   columns, the vacuum is turned on and the sample is pulled through the resin into glass

483   collection vials. The flow through is again passed over the resin to ensure maximal binding of

484   crosslinked amino acids and set aside. The column is then washed with 1.5 mL of fresh 4:1:1

485   organic mixture. A fresh collection vessel is placed under the column and 750 µL of 18 MΩ H2O

486   is used to elute crosslinked amino acids off of the CF-11 resin. The eluent is then placed in a

487   speed vac and run until complete dryness. Dried eluent is then reconstituted in a buffer

488   appropriate for downstream MS analysis on amide HILIC UHPLC columns.

489   **UHPLC analysis**

20

490   Up to 20 μL of tissue hydrolysates were analyzed on a Vanquish UPHLC system

491   (ThermoFisher, San Jose, CA, USA) using an Acquity UHPLC BEH Amide column (2.1 x

492   100mm, 1.7 μm particle size – Waters, Milford, MA, USA). Samples were separated using a 5

493   minute gradient elution (55% - 40% Mobile phase B) at 250 μL/min (mobile phase: (A) 10mM

494   ammonium acetate adjusted to pH 10.2 with NH₄OH (B) 95% acetonitrile, 5% Mobile Phase A,

495   pH 10.2, column temperature: 35°C.

496   **MS data acquisition**

497   The Vanquish UPHLC system (ThermoFisher, San Jose, CA, USA) was coupled online with a

498   QExactive mass spectrometer (Thermo, San Jose, CA, USA), and operated in two different

499   modes – 1. Full MS mode (2 μscans) at 70,000 resolution from 75 to 600 m/z operated in

500   positive ion mode and 2. PRM mode at 17,500 resolution with an inclusion list of in-tact

501   crosslinked amino acid masses (Supplementary Table 2), and an isolation window of 4 m/z.

502   Both modes were operated with 4 kV spray voltage, 15 sheath gas and 5 auxiliary gas.

503   Calibration was performed before each analysis using a positive calibration mix (Piercenet –

504   Thermo Fisher, Rockford, IL, USA). Limits of detection (LOD) were characterized by

505   determining the smallest injected crosslinked amino acids (LNL, DHLNL, d-Pyr,) amount

506   required to provide a signal to noise (S/N) ratio greater than three using < 5 ppm error on the

507   accurate intact mass. Based on a conservative definition for Limit of Quantification (LOQ), these

508   values were calculated to be threefold higher than determined LODs.

509   **MS data analysis**

510   MS Data acquired from the QExactive were converted from a raw file format to .mzXML format

511   using MassMatrix (Cleveland, OH, USA). Assignment of crosslinked amino acids was performed

512   using MAVEN (Princeton, NJ, USA)(58). The MAVEN software platform provides the means to

513   evaluate data acquired in Full MS and PRM modes and the import of in-house curated peak lists

514   for rapid validation of features. Normalization of crosslinked amino acid peak areas was

515   performed using two parameters, 1. Hydroxy proline content and 2. Tissue dry weight pre-

516   hydrolysis (in milligrams)(57). Hydroxy proline content is determined by running a 1:10 dilution

517   of the pre-enrichment sample through the Full MS mode (only) described above and exporting

518   peak areas for each run.

519   **Quantification of crosslinked amino acids**

520   Relative quantification of crosslinked amino acids was performed by exporting peak areas from

521   MAVEN into GraphPad (La Jolla, CA, USA) and normalizing based on the two parameters

522   described above. Statistical analysis, including T test and ANOVA (significance threshold for P

523   values <0.05) were performed on normalized peak areas. Total crosslink plots were generated

524   by summing normalized peak areas for all crosslinks in a given sample. Total HLCC plots were

525   generated by summing normalized peak areas for all HLCC (DHLNL, Pyr, dPyr) crosslinks in a

526   given sample.

527   **Picrosirius red staining and quantification**

528   FFPE tissue sections were stained using 0.1% Picrosirius red (Direct Red 80, Sigma-Aldrich,

529   Cat# 365548 and picric acid solution, Sigma-Aldrich, Cat# P6744) and counterstained with

530   Weigert's hematoxylin (Cancer Diagnostics, Cat# CM3951), as previously described(2).

531   Polarized light images were acquired using an Olympus IX81 microscope fitted with an analyzer

532   (U-ANT) and a polarizer (U-POT, Olympus) oriented parallel and orthogonal to each other.

533   Images were quantified using an ImageJ macro to determine percentage area coverage per

534   field of view. The ImageJ macro is available at https://github.com/northcottj/picrosirius-red.

535   **Second harmonic generation image acquisition**

536   Second harmonic generation (SHG) imaging was performed using a custom-built two-photon

537   microscope setup equipped resonant-scanning instruments based on published designs

538   containing a five-PMT array (Hamamatsu, C7950), as previously published(2). The setup was

539   used with two channel simultaneous video rate acquisition via two PMT detectors and an

540   excitation laser (2W MaiTai Ti-Sapphire laser, 710–920 nm excitation range). SHG imaging was

541   performed on a Prairie Technology Ultima System attached to an Olympus BX-51 fixed stage

542   microscope equipped with a 25X (NA 1.05) water immersion objective. Paraformaldehyde-fixed

543   or FFPE tissue sections were exposed to polarized laser light at a wavelength of 830 nm and

544   emitted light was separated using a filter set (short pass filter, 720 nm; dichroic mirror, 495 nm;

545   band pass filter, 475/40 nm). Images of x–y planes at a resolution of 0.656 mm per pixel were

546   captured using at open-source Micro-Magellan software suite.

547   **Immunofluorescence/Immunohistochemistry**

548   Immunofluorescence staining was performed as previously described(2). Briefly, mouse tissues

549   were harvested and fixed with 10% buffered formalin phosphate (Fisher, Cat# 100-20) for 16-24

550   hours at room temperature and then further processed and paraffin-embedded. Five-μm

551   sections dried for 30 minutes in 60°C, follow by deparaffinization and rehydration. Antigen

552   retrieval was perform using DAKO Target Retrieval Solution (DAKO, Cat# S1699) for five

553   minutes in a pressure cooker set to high pressure. Tissue sections were incubated with anti-

554   FAK pY397 antibody (Abcam, Cat# Ab39967, dilution 1:25) overnight at 4°C and with anti-rabbit

555   IgG Alex Fluor 633 (ThermoFisher, Cat# A-21070, dilution 1:2000) for one hour at room

556   temperature. Antigen retrieval for immunofluorescent staining of SMAD2 pS465/467,

557   cytokeratin 8+18, cytokeratin 5, F4/80, vimentin, and PDGFRα was performed using Diva

558   Decloaker (BioCare, Cat# DV2004MX) for five minutes in a pressure cooker set to high

559   pressure. Tissue sections were incubated with anti-SMAD2 pS465/467 antibody (Millipore, Cat#

560   AB3849-I, dilution 1:100), anti-F4/80 antibody (AbD Serotec, clone CI:A3-1, Cat# MCA497GA,

561   dilution 1:400), anti-cytokeratin 8+18 antibody (Fitzgerald, Cat# 20R-CP004, dilution 1:400),

562   anti-cytokeratin 5 antibody (Fitzgerald, Cat# 20R-CP003, dilution 1:400), anti-vimentin antibody

563   (Cell Signaling, Cat# 5741, dilution 1:100), and anti-PDGFRα (CD140a) antibody (Biolegend,

564   Cat# 135901, dilution 1:100) overnight at 4°C and with anti-rat IgG Alex Fluor 488

565   (ThermoFisher, Cat# A-11006, dilution 1:1000), anti-guinea pig IgG Alex Fluor 568

566   (ThermoFisher, Cat# A-11075, dilution 1:1000), anti-rabbit IgG Alex Fluor 633 (ThermoFisher,

567   Cat# A-21070, dilution 1:2000), anti-rabbit IgG Alex Fluor 633 (ThermoFisher, Cat# A-21070,

568   dilution 1:1000) for one hour at room temperature.

569   Quantification of stromal nuclear SMAD2 pS465/467 was performed using Imaris 9. Surfaces

570   were created around each nucleus and epithelial nuclei were manually excluded based on

571   cytokeratin signal and cell morphology. The means of the mean nuclear signal intensity for all

572   stromal nuclei were calculated for each field of view and averaged for every animal.

573   Lungs from 11 week old IgG1 control and anti-CSF1 treated PyMT mice were cut into 5 micron

574   sections from 5 layers with 100 microns between the first three layers and 50 microns between

575   the last two layers. Sections were analyzed for metastases by PyMT staining. Antigen retrieval

576   was performed in Tris-EDTA buffer at pH 9 for four minutes in a pressure cooker set to low

577   pressure. Tissue sections were incubated with anti-PyMT antibody (Novus Biologicals, Cat# NB-

578   100-2749, dilution 1:250) overnight at 4°C and with a biotinylated anti-rat antibody for 1 hour at

579   room temperature. Vectastain Elite ABC (Vector, Cat# PK6100) and ImmPACT DAB Peroxidase

580   (Vector, Cat# SK-4105) were used for signal detection and nuclei were counterstained with

581   methyl green.

582   **mRNA In Situ Hybridization**

583   Fresh, RNase-free FFPE sections were stained with RNAscope multiplex fluorescent reagent kit

584   V2 according to standard manufacturer protocol. Target retrieval was performed using 8 minute

585   incubation in a pressure cooker set to low pressure. Opal 520 and Opal 570 (PerkinElmer) were

586   used at 1:1500 for target visualization.

587   **Gene expression by RT-qPCR**

Total RNA was reverse-transcribed using random primers (Amersham Bioscienes) and results

were normalized to 18S RNA to control for varying cDNA concentration between samples. The

primer sequences used are 18s forward 5'-GGATGCGTGCATTTATCAGA-3' and reverse 5'-

GGCGACTACCATCGAAAGTT-3', Lox forward 5'-CGGGAGACCGTACTGGAAGT-3' and

24

reverse 5'-CCCAGCCACATAGATCGCAT-3', Loxl2 forward 5'-CACAGGCACTACCACAGCAT-

3' and reverse 5'-CCAAAGTTGGCACACTCGTA-3', and Tgfb1 forward 5'-

TCATGTCATGGATGGTGCCC-3' and reverse 5'-GTCACTGGAGTTGTACGGCA-3'.

Atomic force microscopy data acquisition

Atomic force microscopy (AFM) measurements were performed as previously described(2).

Briefly, 20µm OCT-embedded frozen human breast tissue or 30µm mouse mammary gland

sections were fast thawed by immersion in PBS at room temperature. Next, these sections were

immersed in PBS containing phosphatase inhibitors (Roche, Cat# 04906845001), protease

inhibitor (Roche, Cat# 04693124001), and propidium iodide (ACROS, Cat# 440300250) and

placed on the stage for AFM measurements. AFM indentations were performed using an

MFP3D-BIO inverted optical AFM (Asylum Research) mounted on a Nikon TE2000-U inverted

fluorescent microscope. Silicon nitride cantilevers were used with a spring constant of 0.06 N m^{-1} and a borosilicate glass spherical tip with 5 µm diameter (Novascan Tech). The cantilever was

calibrated using the thermal oscillation method prior to each experiment. The indentation rate

was held constant within each study but varied between 2-20 µms^{-1} with a maximum force of 2

nN between studies. Force maps were obtained as a raster series of indentations utilizing the

FMAP function of the IGOR PRO build supplied by Asylum Research. Elastic properties of ECM

were reckoned using the Hertz model. A Poisson's ratio of 0.5 was used in the calculation of the

Young's elastic modulus.

Western blotting

Snap frozen tissues were ground while frozen and lysed in 2% SDS containing protease and

phosphatase inhibitor. Samples were boiled for 5 minutes (95°C) and loaded onto the SDS-

polyacrylamide gel, and protein was separated at 110 constant volts.

The protein was transferred onto a pre-wet polyvinylidene difluoride (PVDF) membrane (100%

methanol, 1 minute) at 250 mA for 2 hours. The PVDF membrane was rinsed with TBST and

25

610   non-specific binding was blocked with 5% nonfat dry milk dissolved in TBST. The membrane

611   was then incubated with the primary antibody overnight at 4°C, washed with TBST, incubated

612   with horseradish-peroxidase conjugated secondary antibody (1 hour, room temperature; dilution

613   1:5000), washed with TBST, and detected with the chemiluminescence system Quantum HRP

614   substrate (Advansta #K-12042). Quantification was performed using gel densitometry in

615   ImageJ. Primary antibodies used are anti-LOX (1:1000, Abcam Cat# ab174316) and anti-E-

616   cadherin (1:1000, Cell Signlaing Cat#3195).

617   **Flow cytometry**

618   Mouse tissue was harvested and chopped with a razor blade. Chopped tissue was digested in

619   100 U/mL Collagenase Type 1 (Worthington Biochemical Corporation, Cat# LS004196), 500

620   U/mL Collagenase Type 4 (Worthington Biochemical Corporation, Cat# LS004188), and 200

621   µg/mL DNase I (Roche, Cat# 10104159001) while shaking at 37°C. Digested tissue was filtered

622   using a 100 µm filter to remove remaining pieces. Red blood cells were lysed in ammonium-

623   chloride-potassium buffer and remaining cells were counted. Cells were stained with

624   fluorophore-conjugated primary antibodies for 30 minutes on ice and subsequently stained with

625   a viability marker. Antibodies used for staining were anti-mouse CD24-PE (BD Pharmingen,

626   Cat# 553262), anti-mouse TER-119-APC (BioLegend, Cat# 116212), anti-mouse CD45-APC

627   (BioLegend, Cat# 103112), anti-mouse CD29-AF700 (BioLegend, Cat# 102218), anti-mouse

628   Ly6G-BV421 (BioLegend, Cat# 127628), anti-mouse F4/80-BV510 (BioLegend, Cat# 123135),

629   anti-mouse CD29-AF488 (BioLegend, Cat# 102212), anti-mouse CD140a-PE (BioLegend, Cat#

630   135906), anti-mouse CD31-APC (BioLegend, Cat# 102410), anti-mouse CD11c-BV605 (BD

631   Pharmingen, Cat# 563057), anti-mouse CD24-BV650 (BD Pharmingen, Cat# 563545), anti-

632   mouse CD11b-PerCP-Cy5.5 (eBiosciences, Cat# 45-0112-82), anti-mouse CD45-AF700

633   (BioLegend, Cat# 103128), anti-mouse Ly6C-BV711 (BioLegend, Cat# 128037), anti-mouse

26

634   MHCII-PE-Cy7 (BioLegend, Cat# 107630), and Zombie NIR Fixable Viability Dye (BioLegend,

635   Cat# 423105). Cells were then analyzed on a flow cytometer.

636   **Patient gene expression analysis**

637   For the stroma and epithelium specific gene expression analysis, the breast cancer datasets

638   from Finak *et al.* 2008 and Gruosso *et al.* 2019 have been used. Briefly, whole Human Genome

639   44 K arrays (Agilent Technologies, product G4112A) were used for stroma and epithelial

640   expression profiles. Details of laser capture microdissection, RNA extraction, labeling,

641   hybridization, scanning and quality filters are described in Finak *et al.,* 2006 and 2008. Briefly,

642   the dataset was normalized using loess (within-array) and quantile (between-array)

643   normalization. Probes were ranked by Inter-quartile range (IQR) values, and the most variable

644   probe per gene across expression data were selected for further analysis. Replicate arrays with

645   a concordance above 0.944 were averaged before assessing differential expression.

646   An association between PLOD2 and distant metastasis-free survival (DMFS) has been

647   determined using an online tool (http://xena.ucsc.edu) to download GEO data (GSE2034,

648   GSE5327, and GSE7390) from 683 patients analyzed on Affymetrix U133A platform as

649   described in Yau et al.(46). Patients have been excluded from analyses if their molecular

650   subtyping of ER/HER2 status and PAM50 did not align: ER+/HER2- must always be luminal,

651   ER+ or-/HER2+ must be HER2+, and ER-/HER2- must always be basal-like. PLOD2 expression

652   levels have been divided based on the median for each tumor subtype: ER+/HER2- (low n=157;

653   high=157), ER- or +/HER2+ (low n=36; high=37), and ER-/HER2- (low n=66; high=67). All

654   statistical analyses were done using GraphPad Prism Version 6.01: Kruskal-Wallis one-way

655   ANOVA test was applied to assess the relationship in PLOD2 expression levels among tumor

656   subtypes and log rank P value (Mantel-Cox) tests for DMFS curves.

657   An association between PLOD2 gene expression and relapse-free survival (RFS) has been

658   determined using an online tool (http://kmplot.com/analysis/) from 1,809 patients analyzed on

27

659   Affymetrix platform (HGU133A and HGU133+2 microarrays)(47). Affymetrix ID 202619 or

660   202620 were used for PLOD2 probes (2014 version) in these analyses. All breast cancer

661   patients in this database were included regardless to lymph node status, TP53 status, or grade.

662   No restrictions were placed in term of patient treatment. PLOD2 expression levels have been

663   divided based on the median for each tumor subtype: ER+/PR+/HER2- (low n=170; high=169),

664   ER-/PR-/HER2+ (low n=58; high=57), and ER-/PR-/HER- (low n=128; high=127). Hazard ratio

665   (and 95% confidence intervals) and log rank P values were calculated and displayed once the

666   data were plotted using the online tool.

667   The cBioPortal for Cancer Genomics was used to determine the levels of LOX, PLOD2, and

668   LOXL2 gene expression in breast cancer patients segregated by ER and HER2 status(59,60).

669   ER, PR, and HER2 status were determined by gene expression levels. Samples positive for

670   both ER/PR and HER2 overexpression were excluded from subtype analysis. The cBioPortal

671   was also used to assess gene expression associations of LOX, PLOD2, and LOXL2 with HIF1A,

672   CCL2, CD163, and CD68. All data accessed via cBioPortal are from the 1904 patients in the

673   METABRIC dataset analyzed for gene expression by Illumina human v3 microarray(61). All

674   1904 samples were included in correlation analyses.

675   **Statistical analysis**

676   GraphPad Prism Version 6.01 was used to perform all statistical analyses with the exception of

677   LH2 IHC and RFS correlations with PLOD2. Statistical significance was determined using the

678   appropriate tests as noted in the figure legends or method section.

679   **LH2 IHC and prognostic analyses:**

680   *Study population*

681   The female Malmö Diet and Cancer Study (MDCS) cohort consists of women born 1923–

682   1950)(62,63). Information on incident breast cancer is annually retrieved from the Swedish

683   Cancer Registry and the South Swedish Regional Tumor Registry. Follow-up until December

684   31, 2010, identified a total of 910 women with incident breast cancer, the following conditions

28

685 excluded patients: 1) with in situ only cancers (n=68), 2) who received neo-adjuvant treatments

686 (n=4), 3) with distant metastasis at diagnosis (n=14), 4) those who died from breast cancer-

687 related causes ≤ 0.3 years from diagnosis (n=2), and finally 5) patients with bilateral cancers

688 (n=17). In addition, one patient who declined treatment for four years before accepting surgery

689 was excluded. Patient characteristics at diagnosis and pathological tumor data were obtained

690 from medical records. Information on cause of death and vital status was retrieved from the

691 Swedish Causes of Death Registry, with last follow-up December 31st, 2014. Ethical permission

692 was obtained from the Ethical Committee at Lund University (Dnr 472/2007). All participants

693 originally signed a written informed consent form.

694 *Tumor evaluation*

695 Tumor samples from incident breast cancer cases in MDCS were collected, and a tissue

696 microarray (TMA) including two 1-mm cores from each tumor was constructed (Beecher, WI,

697 USA). Within the study population (N=910), tumor tissue cores were accessible from 718

698 patients. Four-μm sections dried for one hour in 60°C were automatically pretreated using the

699 Autostainer plus, DAKO staining equipment with Dako kit K8010 (Dako, DK). A primary mouse

700 monoclonal Lysyl Hydroxylase 2 (LH2) antibody (Origene; Cat# TA803224, dilution 1:150) was

701 used for the immunohistochemical staining.

702 TMA cores were analyzed by a cohort of 4 anatomic pathologists (ACN, AC, JG, AN) using the

703 PathXL digital pathology system (http://www.pathxl.com, PathXL Ltd., UK) blinded to all other

704 clinical and pathologic variables. Immunohistochemistry for LH2 was assessed separately for

705 stromal and neoplastic epithelial components of the tumors. Stromal LH2 staining was assessed

706 with the semi-quantitative H-score which combines intensity and proportion positive

707 assessments into a continuous variable from 0-300(64). Cellular stromal components were

708 assessed (including fibroblasts, macrophages, endothelial cells, adipocytes, and other stromal

709 cell types) while areas of significant lymphocytic infiltrate were specifically excluded from the

710 percent positive estimation. Neoplastic epithelial LH2 staining intensity was scored 0-3+ based

29

711   on the predominant intensity pattern in the tumor — invasive tumor cells did not display

712   significant intra-tumoral heterogeneity of LH2 staining within each core. Verification of inter-

713   observer reproducibility for the H-score was established in a training series of 16 cases

714   evaluated by all study pathologists to harmonize scoring. Inter-observer agreement in the

715   training set was very high, evaluating the IHC scores both as continuous variables (Pearson

716   correlation coefficients ranging from 0.912-0.9566, all p values < 0.0001), and after

717   transformation into categorical data (negative, low, and moderate/high; weighted kappa

718   coefficients ranging from 0.673-0.786). In addition, 50 cases of the study cohort were evaluated

719   blindly by two pathologists to confirm data fidelity; the Pearson correlation coefficient = 0.7507

720   (p = 5.7 E-05), considered a strong level of agreement.

721   After exclusion of cases for which LH2 was not evaluable on the TMA, H-scores for 505 patients

722   were included for statistical associations with clinicopathologic features and patient outcome.

723   Each patient was represented by two cores, and TMA core 1 and core 2 were merged into a

724   joint variable favoring the highest stromal LH2 H-score or epithelial LH2 intensity because we

725   predict that higher H-score would drive patient outcome in accordance with our gene expression

726   data demonstrating high LH2 expression correlated with poor outcome. The Pearson correlation

727   coefficient between cores = 0.647, demonstrating moderate agreement among the stromal LH2

728   H-scores for the two cores. In cases with only one TMA core providing a LH2 score, the

729   expression of this core was used. Further, the joint stromal LH2 variable was categorized into

730   tertiles based on the study population with valid LH2 annotation (N=505). The lowest tertile of

731   LH2 H-scores were defined as scores between 0 and less or equal to 120 (N=171), the

732   intermediate H-score as above 120 and equal or less than 230 (N=188), and the highest stromal

733   LH2 score as above 230 (N=146).

734   *Statistical analyses for LH2 IHC analyses*

735   Patient and tumor characteristics at diagnosis in relation to stromal LH2 expression were

736   categorized and presented as percentages. Continuous variables are presented as the mean

737 and min/max. The associations between LH2 expression and grade or tumor size, respectively,

738 were analyzed through linear-by-linear association. The association between LH2 expression

739 and prognosis was examined using breast cancer-specific mortality as endpoint, which was

740 defined as the incidence of breast cancer-related death. Follow-up was calculated from the date

741 of breast cancer diagnosis to the date of breast cancer-related death, date of death from

742 another cause, date of emigration or the end of follow-up as of December 31st, 2014. Main

743 analyses included the overall population; additional analyses were performed in subgroup

744 analyses stratified by estrogen receptor (ER) or axillary lymph node involvement (ALNI) status.

745 The prognostic impact of stromal LH2 expression was analyzed through Cox proportional

746 hazards analyses, which yielded hazard ratios (HR) and 95% confidence intervals (CI) for crude

747 models, and multivariate models adjusted for age at diagnosis (model 1) and tumor

748 characteristics ER (dichotomized, cut-off 10% stained nuclei), ALNI (none or any positive lymph

749 node involvement), histological grade (Nottingham grade I-III), and tumor size (dichotomized

750 using cut-off 20 mm). Kaplan-Meier curves including the LogRank test indicated LH2 status to

751 particularly impact the first 10 years after diagnosis and survival variables constructed to

752 capture these effects were used in Cox regression models investigating the effects during the

753 first post-diagnostic decade. All statistical analyses were performed in SPSS version 22.0

754 (IBM).

755

Author Contributions

V.M.W., K.C.H., O.M., A.S.B., and A.P.D. conceived the project, prepared figures and wrote the manuscript. A.S.B, T.P., T.N., and K.C.H. developed the xAAA method and A.S.B performed all LC-MS and LC-PRM experiments. J.N.L generated the TetO_mLOX mouse model. O.M. designed and conducted *in vivo* experiments using inducible LOX overexpression models. B.R. and L.C. designed and conducted CSF1 blocking antibody mouse experiment. O.M. and A.P.D. performed and quantified immunofluorescence, H&E, PS and SHG imaging and analyses on mouse tissue samples. I.A., A.P.D., and J.M.B performed AFM on human or mouse tissue specimens. I.A. performed SHG imaging on human tissue. E.S.H, and P.K. provided human breast tumor biopsies for xAAA. B.R. and L.C. designed and conducted immunoprofiling on human breast tumor via flow cytometry. O.M. and A.P.D. performed all gene expression analyses with the exception of Fig. 5g-j. T.G, H.K. and M.P. performed gene expression analyses gene expression in microdissected epithelial and stromal compartments of human invasive breast carcinomas. O.M. and A.P.D. designed and conducted *in vivo* experiments using minoxidil treatment. S.B. established and managed MDCS cohort used for LH2 IHC. Z.W. and S.B. performed LH2 IHC. A.C.N. designed scoring schemes for stromal and neoplastic epithelial LH2 IHC, and A.C.N, A.N., J.G., and A.C. scored all human biopsies. S.B., O.B., A.C.N., O.M., and V.M.W analyzed and interpreted clinical data from LH2 scores.

References:

785   1.   Laklai H, Miroshnikova YA, Pickup MW, Collisson EA, Kim GE, Barrett AS, *et al.*
786   Genotype tunes pancreatic ductal adenocarcinoma tissue tension to induce matricellular
787   fibrosis and tumor progression. Nat Med **2016**;22(5):497-505 doi 10.1038/nm.4082.
788   2.   Acerbi I, Cassereau L, Dean I, Shi Q, Au A, Park C, *et al.* Human breast cancer invasion
789   and aggression correlates with ECM stiffening and immune cell infiltration. Integr Biol
790   (Camb) **2015**;7(10):1120-34 doi 10.1039/c5ib00040h.
791   3.   Dvorak HF. Tumors: wounds that do not heal. Similarities between tumor stroma
792   generation and wound healing. N Engl J Med **1986**;315(26):1650-9 doi
793   10.1056/NEJM198612253152606.
794   4.   Conklin MW, Eickhoff JC, Riching KM, Pehlke CA, Eliceiri KW, Provenzano PP, *et al.*
795   Aligned collagen is a prognostic signature for survival in human breast carcinoma. The
796   American journal of pathology **2011**;178(3):1221-32 doi 10.1016/j.ajpath.2010.11.076.
797   5.   Olive KP, Jacobetz MA, Davidson CJ, Gopinathan A, McIntyre D, Honess D, *et al.*
798   Inhibition of Hedgehog signaling enhances delivery of chemotherapy in a mouse model
799   of pancreatic cancer. Science **2009**;324(5933):1457-61 doi 10.1126/science.1171362.
800   6.   Provenzano PP, Cuevas C, Chang AE, Goel VK, Von Hoff DD, Hingorani SR. Enzymatic
801   targeting of the stroma ablates physical barriers to treatment of pancreatic ductal
802   adenocarcinoma. Cancer Cell **2012**;21(3):418-29 doi 10.1016/j.ccr.2012.01.007.
803   7.   Netti PA, Berk DA, Swartz MA, Grodzinsky AJ, Jain RK. Role of extracellular matrix
804   assembly in interstitial transport in solid tumors. Cancer Res **2000**;60(9):2497-503.
805   8.   Jain RK, Lee JJ, Hong D, Kurzrock R. Reply to A. Levy et al. J Clin Oncol
806   **2013**;31(3):396 doi 10.1200/JCO.2012.46.4867.
807   9.   Egeblad M, Rasch MG, Weaver VM. Dynamic interplay between the collagen scaffold
808   and tumor evolution. Curr Opin Cell Biol **2010**;22(5):697-706 doi
809   10.1016/j.ceb.2010.08.015.
810   10.   Chaudhuri O, Koshy ST, Branco da Cunha C, Shin JW, Verbeke CS, Allison KH, *et al.*
811   Extracellular matrix stiffness and composition jointly regulate the induction of malignant
812   phenotypes in mammary epithelium. Nat Mater **2014**;13(10):970-8 doi
813   10.1038/nmat4009.
814   11.   Provenzano PP, Inman DR, Eliceiri KW, Keely PJ. Matrix density-induced
815   mechanoregulation of breast cell phenotype, signaling and gene expression through a
816   FAK-ERK linkage. Oncogene **2009**;28(49):4326-43.
817   12.   Levental KR, Yu H, Kass L, Lakins JN, Egeblad M, Erler JT, *et al.* Matrix crosslinking
818   forces tumor progression by enhancing integrin signaling. Cell **2009**;139(5):891-906.
819   13.   Mekhdjian AH, Kai F, Rubashkin MG, Prahl LS, Przybyla LM, McGregor AL, *et al.*
820   Integrin-mediated traction force enhances paxillin molecular associations and adhesion
821   dynamics that increase the invasiveness of tumor cells into a three-dimensional
822   extracellular matrix. Mol Biol Cell **2017**;28(11):1467-88 doi 10.1091/mbc.E16-09-0654.
823   14.   Pickup MW, Laklai H, Acerbi I, Owens P, Gorska AE, Chytil A, *et al.* Stromally derived
824   lysyl oxidase promotes metastasis of transforming growth factor-beta-deficient mouse
825   mammary carcinomas. Cancer Res **2013**;73(17):5336-46 doi 10.1158/0008-5472.CAN-
826   13-0012.

827   15.   Pickup MW, Mouw JK, Weaver VM. The extracellular matrix modulates the hallmarks of
828   cancer. EMBO Rep **2014**;15(12):1243-53 doi 10.15252/embr.201439246.
829   16.   Provenzano PP, Inman DR, Eliceiri KW, Knittel JG, Yan L, Rueden CT*, et al.* Collagen
830   density promotes mammary tumor initiation and progression. BMC Med **2008**;6:11 doi
831   1741-7015-6-11 [pii]

832   10.1186/1741-7015-6-11.
833   17.   Eyre DR, Weis MA, Wu J-J. Advances in collagen cross-link analysis. Methods
834   **2008**;45(1):65-74.
835   18.   Mammoto T, Ingber DE. Mechanical control of tissue and organ development.
836   Development **2010**;137(9):1407-20.
837   19.   Yamauchi M, Shiiba M. Lysine hydroxylation and cross-linking of collagen. Post-
838   translational Modifications of Proteins **2008**:95-108.
839   20.   Yamauchi M, Sricholpech M. Lysine post-translational modifications of collagen. Essays
840   in biochemistry **2012**;52:113-33.
841   21.   Miller BW, Morton JP, Pinese M, Saturno G, Jamieson NB, McGhee E*, et al.* Targeting
842   the LOX/hypoxia axis reverses many of the features that make pancreatic cancer
843   deadly: inhibition of LOX abrogates metastasis and enhances drug efficacy. EMBO Mol
844   Med **2015**;7(8):1063-76 doi 10.15252/emmm.201404827.
845   22.   Erler JT, Weaver VM. Three-dimensional context regulation of metastasis. Clin Exp
846   Metastasis **2009**;26(1):35-49 doi 10.1007/s10585-008-9209-8.
847   23.   Chen Y, Terajima M, Yang Y, Sun L, Ahn Y-H, Pankova D*, et al.* Lysyl hydroxylase 2
848   induces a collagen cross-link switch in tumor stroma. The Journal of clinical investigation
849   **2015**;125(3):1147.
850   24.   Gilkes DM, Bajpai S, Wong CC, Chaturvedi P, Hubbi ME, Wirtz D*, et al.* Procollagen
851   lysyl hydroxylase 2 is essential for hypoxia-induced breast cancer metastasis. Molecular
852   cancer research **2013**;11(5):456-66.
853   25.   Erler JT, Bennewith KL, Nicolau M, Dornhofer N, Kong C, Le QT*, et al.* Lysyl oxidase is
854   essential for hypoxia-induced metastasis. Nature **2006**;440(7088):1222-6 doi
855   10.1038/nature04695.
856   26.   Lampi MC, Reinhart-King CA. Targeting extracellular matrix stiffness to attenuate
857   disease: From molecular mechanisms to clinical trials. Sci Transl Med **2018**;10(422) doi
858   10.1126/scitranslmed.aao0475.
859   27.   Grivennikov SI, Greten FR, Karin M. Immunity, inflammation, and cancer. Cell
860   **2010**;140(6):883-99 doi 10.1016/j.cell.2010.01.025.
861   28.   Mack M. Inflammation and fibrosis. Matrix Biol **2018**;68-69:106-21 doi
862   10.1016/j.matbio.2017.11.010.
863   29.   Wick G, Grundtman C, Mayerl C, Wimpissinger TF, Feichtinger J, Zelger B*, et al.* The
864   immunology of fibrosis. Annu Rev Immunol **2013**;31:107-35 doi 10.1146/annurev-
865   immunol-032712-095937.
866   30.   Ueha S, Shand FH, Matsushima K. Cellular and molecular mechanisms of chronic
867   inflammation-associated organ fibrosis. Front Immunol **2012**;3:71 doi
868   10.3389/fimmu.2012.00071.
869   31.   Sun X, Glynn DJ, Hodson LJ, Huo C, Britt K, Thompson EW*, et al.* CCL2-driven
870   inflammation increases mammary gland stromal density and cancer susceptibility in a
871   transgenic mouse model. Breast Cancer Res **2017**;19(1):4 doi 10.1186/s13058-016-
872   0796-z.
873   32.   Qian BZ, Li J, Zhang H, Kitamura T, Zhang J, Campion LR*, et al.* CCL2 recruits
874   inflammatory monocytes to facilitate breast-tumour metastasis. Nature
875   **2011**;475(7355):222-5 doi 10.1038/nature10138.

876 33. Lohela M, Casbon AJ, Olow A, Bonham L, Branstetter D, Weng N, *et al.* Intravital
877   imaging reveals distinct responses of depleting dynamic tumor-associated macrophage
878   and dendritic cell subpopulations. Proc Natl Acad Sci U S A **2014**;111(47):E5086-95 doi
879   10.1073/pnas.1419899111.
880 34. Ruffell B, Chang-Strachan D, Chan V, Rosenbusch A, Ho CM, Pryer N, *et al.*
881   Macrophage IL-10 blocks CD8+ T cell-dependent responses to chemotherapy by
882   suppressing IL-12 expression in intratumoral dendritic cells. Cancer Cell **2014**;26(5):623-
883   37 doi 10.1016/j.ccell.2014.09.006.
884 35. DeNardo DG, Brennan DJ, Rexhepaj E, Ruffell B, Shiao SL, Madden SF, *et al.*
885   Leukocyte complexity predicts breast cancer survival and functionally regulates
886   response to chemotherapy. Cancer Discov **2011**;1(1):54-67 doi 10.1158/2159-8274.CD-
887   10-0028.
888 36. Nemkov T, D'Alessandro A, Hansen KC. Three-minute method for amino acid analysis
889   by UHPLC and high-resolution quadrupole orbitrap mass spectrometry. Amino acids
890   **2015**;47(11):2345-57.
891 37. Oxlund H, Barckman M, Ørtoft G, Andreassen T. Reduced concentrations of collagen
892   cross-links are associated with reduced strength of bone. Bone **1995**;17(4):S365-S71.
893 38. Gruosso T, Gigoux M, Manem VSK, Bertos N, Zuo D, Perlitch I, *et al.* Spatially distinct
894   tumor immune microenvironments stratify triple-negative breast cancers. J Clin Invest
895   **2019**;129(4):1785-800 doi 10.1172/JCI96313.
896 39. Finak G, Bertos N, Pepin F, Sadekova S, Souleimanova M, Zhao H, *et al.* Stromal gene
897   expression predicts clinical outcome in breast cancer. Nat Med **2008**;14(5):518-27 doi
898   10.1038/nm1764.
899 40. Salvador F, Martin A, Lopez-Menendez C, Moreno-Bueno G, Santos V, Vazquez-
900   Naharro A, *et al.* Lysyl oxidase-like protein LOXL2 promotes lung metastasis of breast
901   cancer. Cancer Res **2017** doi 10.1158/0008-5472.CAN-16-3152.
902 41. Eyre DR, Paz MA, Gallop PM. Cross-linking in collagen and elastin. Annual review of
903   biochemistry **1984**;53(1):717-48.
904 42. Lin EY, Nguyen AV, Russell RG, Pollard JW. Colony-stimulating factor 1 promotes
905   progression of mammary tumors to malignancy. J Exp Med **2001**;193(6):727-39 doi DOI
906   10.1084/jem.193.6.727.
907 43. Strachan DC, Ruffell B, Oei Y, Bissell MJ, Coussens LM, Pryer N, *et al.* CSF1R
908   inhibition delays cervical and mammary tumor growth in murine models by attenuating
909   the turnover of tumor-associated macrophages and enhancing infiltration by CD8(+) T
910   cells. Oncoimmunology **2013**;2(12):e26968 doi 10.4161/onci.26968.
911 44. Lin EY, Jones JG, Li P, Zhu L, Whitney KD, Muller WJ, *et al.* Progression to malignancy
912   in the polyoma middle T oncoprotein mouse breast cancer model provides a reliable
913   model for human diseases. Am J Pathol **2003**;163(5):2113-26 doi 10.1016/S0002-
914   9440(10)63568-7.
915 45. Takaluoma K, Lantto J, Myllyharju J. Lysyl hydroxylase 2 is a specific telopeptide
916   hydroxylase, while all three isoenzymes hydroxylate collagenous sequences. Matrix
917   biology **2007**;26(5):396-403.
918 46. Yau C, Esserman L, Moore DH, Waldman F, Sninsky J, Benz CC. A multigene predictor
919   of metastatic outcome in early stage hormone receptor-negative and triple-negative
920   breast cancer. Breast Cancer Res **2010**;12(5):R85 doi 10.1186/bcr2753.
921 47. Gyorffy B, Lanczky A, Eklund AC, Denkert C, Budczies J, Li Q, *et al.* An online survival
922   analysis tool to rapidly assess the effect of 22,277 genes on breast cancer prognosis
923   using microarray data of 1,809 patients. Breast Cancer Res Treat **2010**;123(3):725-31
924   doi 10.1007/s10549-009-0674-9.
925 48. Noy R, Pollard JW. Tumor-associated macrophages: from mechanisms to therapy.
926   Immunity **2014**;41(1):49-61 doi 10.1016/j.immuni.2014.06.010.

49. Lin EY, Li JF, Gnatovskiy L, Deng Y, Zhu L, Grzesik DA, *et al.* Macrophages regulate the angiogenic switch in a mouse model of breast cancer. Cancer Res **2006**;66(23):11238-46 doi 10.1158/0008-5472.CAN-06-1278.

50. Gilkes DM, Bajpai S, Chaturvedi P, Wirtz D, Semenza GL. Hypoxia-inducible factor 1 (HIF-1) promotes extracellular matrix remodeling under hypoxic conditions by inducing P4HA1, P4HA2, and PLOD2 expression in fibroblasts. J Biol Chem **2013**;288(15):10819-29 doi 10.1074/jbc.M112.442939.

51. Wong CC, Gilkes DM, Zhang H, Chen J, Wei H, Chaturvedi P, *et al.* Hypoxia-inducible factor 1 is a master regulator of breast cancer metastatic niche formation. Proc Natl Acad Sci U S A **2011**;108(39):16369-74 doi 10.1073/pnas.1113483108.

52. van der Slot AJ, Zuurmond A-M, Bardoel AF, Wijmenga C, Pruijs HE, Sillence DO, *et al.* Identification of PLOD2 as telopeptide lysyl hydroxylase, an important enzyme in fibrosis. Journal of Biological Chemistry **2003**;278(42):40967-72.

53. Lu P, Takai K, Weaver VM, Werb Z. Extracellular matrix degradation and remodeling in development and disease. Cold Spring Harb Perspect Biol **2011**;3(12) doi 10.1101/cshperspect.a005058.

54. Ahn Y, Sanderson BW, Klein OD, Krumlauf R. Inhibition of Wnt signaling by Wise (Sostdc1) and negative feedback from Shh controls tooth number and patterning. Development **2010**;137(19):3221-31 doi 10.1242/dev.054668.

55. Hsiao EC, Boudignon BM, Chang WC, Bencsik M, Peng J, Nguyen TD, *et al.* Osteoblast expression of an engineered Gs-coupled receptor dramatically increases bone mass. Proc Natl Acad Sci U S A **2008**;105(4):1209-14 doi 10.1073/pnas.0707457105.

56. Guy CT, Cardiff RD, Muller WJ. Induction of mammary tumors by expression of polyomavirus middle T oncogene: a transgenic mouse model for metastatic disease. Mol Cell Biol **1992**;12(3):954-61.

57. Avery NC, Sims TJ, Bailey AJ. Quantitative determination of collagen cross-links. Extracellular Matrix Protocols: Second Edition **2009**:103-21.

58. Clasquin MF, Melamud E, Rabinowitz JD. LC-MS Data Processing with MAVEN: A Metabolomic Analysis and Visualization Engine. Current Protocols in Bioinformatics **2012**:14.1. 1-.1. 23.

59. Cerami E, Gao J, Dogrusoz U, Gross BE, Sumer SO, Aksoy BA, *et al.* The cBio cancer genomics portal: an open platform for exploring multidimensional cancer genomics data. Cancer Discov **2012**;2(5):401-4 doi 10.1158/2159-8290.CD-12-0095.

60. Gao J, Aksoy BA, Dogrusoz U, Dresdner G, Gross B, Sumer SO, *et al.* Integrative analysis of complex cancer genomics and clinical profiles using the cBioPortal. Sci Signal **2013**;6(269):pl1 doi 10.1126/scisignal.2004088.

61. Curtis C, Shah SP, Chin SF, Turashvili G, Rueda OM, Dunning MJ, *et al.* The genomic and transcriptomic architecture of 2,000 breast tumours reveals novel subgroups. Nature **2012**;486(7403):346-52 doi 10.1038/nature10983.

62. Berglund G, Elmstahl S, Janzon L, Larsson SA. The Malmo Diet and Cancer Study. Design and feasibility. J Intern Med **1993**;233(1):45-51.

63. Manjer J, Carlsson S, Elmstahl S, Gullberg B, Janzon L, Lindstrom M, *et al.* The Malmo Diet and Cancer Study: representativity, cancer incidence and mortality in participants and non-participants. Eur J Cancer Prev **2001**;10(6):489-99.

64. Cohen DA, Dabbs DJ, Cooper KL, Amin M, Jones TE, Jones MW, *et al.* Interobserver agreement among pathologists for semiquantitative hormone receptor scoring in breast carcinoma. Am J Clin Pathol **2012**;138(6):796-802 doi 10.1309/AJCP6DKRND5CKVDD.
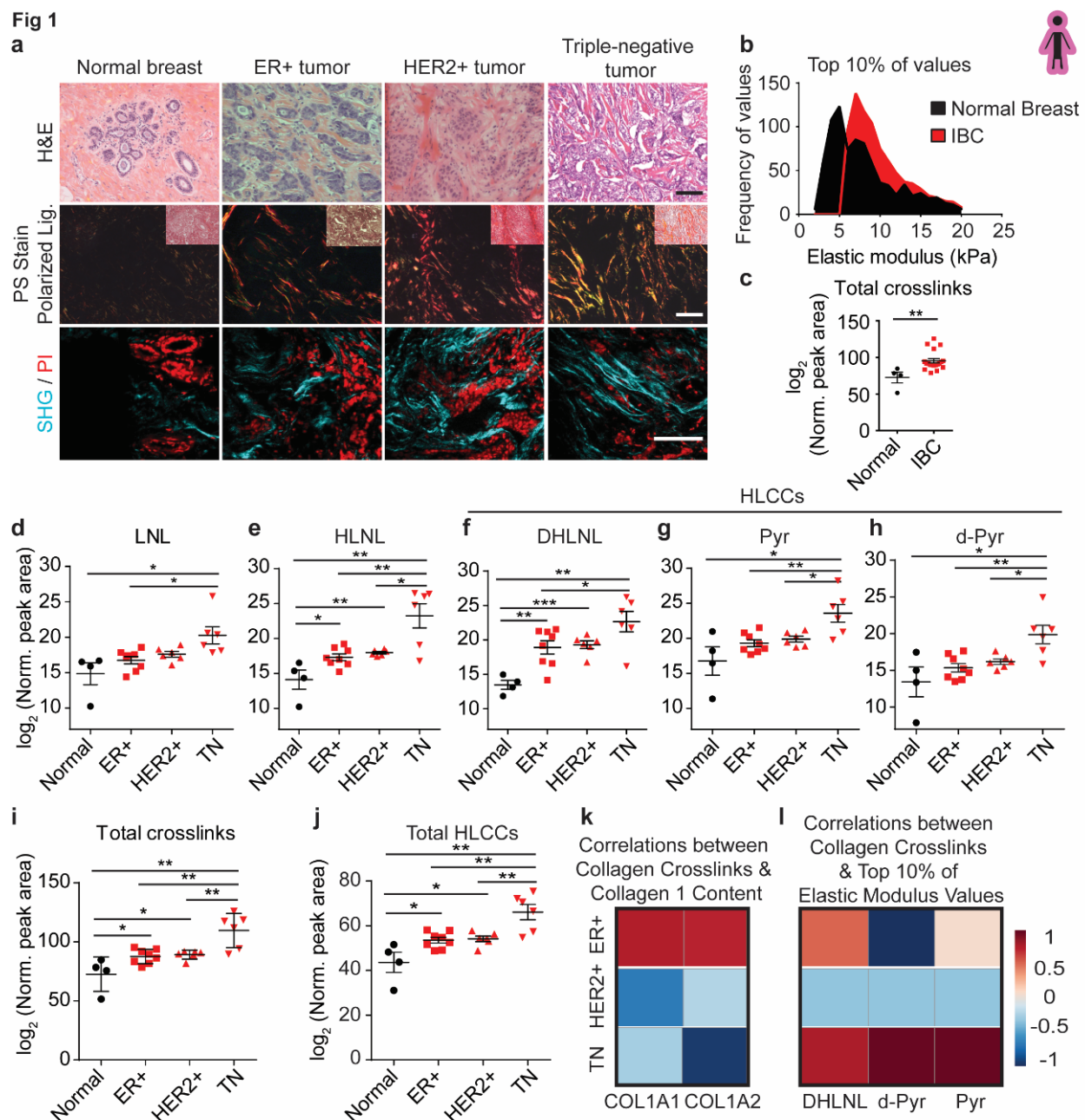
Figure 1: Hydroxylysine collagen crosslink abundance correlates with human breast cancer aggression (**a**) Representative images of normal breast tissue (normal breast; n = 4) and invasive tumors diagnosed as estrogen receptor positive (ER+ tumor; n = 8), epidermal growth factor receptor two positive (HER2+ tumor; n = 6) and triple negative (TN tumor; n = 6). (**Top row**) Brightfield images of human breast tissue stained with hematoxylin and eosin (H&E). (**Middle row**) Polarized light images of picrosirius red (PS) stained human breast tissue with an inset brightfield image shows relative levels of fibrillar collagen. (**Bottom row**) Two photon second harmonic generation (SHG) images of human breast tissue revealing collagen organization

(turquoise) and propidium iodide (PI; red) stained nuclei. Scale bar, 100 μm. (**b**) The distribution of the top 10% of elastic modulus values of normal breast tissue (n = 10) and invasive breast carcinoma (IBC; n = 10) measured by AFM microindentation. Statistical analysis was performing using Mann-Whitney U test (****p < 0.0001). (**c**) Quantification of the abundance of all detected collagen crosslinks in normal breast tissue (n = 4) and in IBC tissues (n = 19) plotted as a scatter plot of individual samples with mean ± SEM. Statistical analysis was performed using Mann-Whitney U test (**p < 0.01). (**d-h**) Scatter plots showing individual and mean values ± SEM of the levels of each LCC and HLCC crosslink measured in normal breast tissues, and in ER+, HER2+ and TN breast tumors. The total abundance of crosslinks (**i**) was calculated by summing all individual crosslinks and the total tissue HLCC abundance (**j**) was calculated by summing DHLNL, Pyr, and d-Pyr and plotted as individual and mean values ± SEM. All crosslink values are normalized to total collagen content (i.e. hydroxyproline abundance) and wet tissue weight and are plotted as $\log_2$ transformed normalized peak areas from LC-MS data. Statistical analysis of crosslinks was performed using one-way ANOVA test for overall analysis and unpaired t-test was used for individual comparisons (*p < 0.05; **p < 0.01). (**k,l**) Heat maps of Spearman correlation coefficients indicating correlations between levels of total collagen crosslinks and collagen I content (**k**) and between levels of each HLCC and the top 10% of elastic modulus measurements (**l**) stratified by tumor subtype.
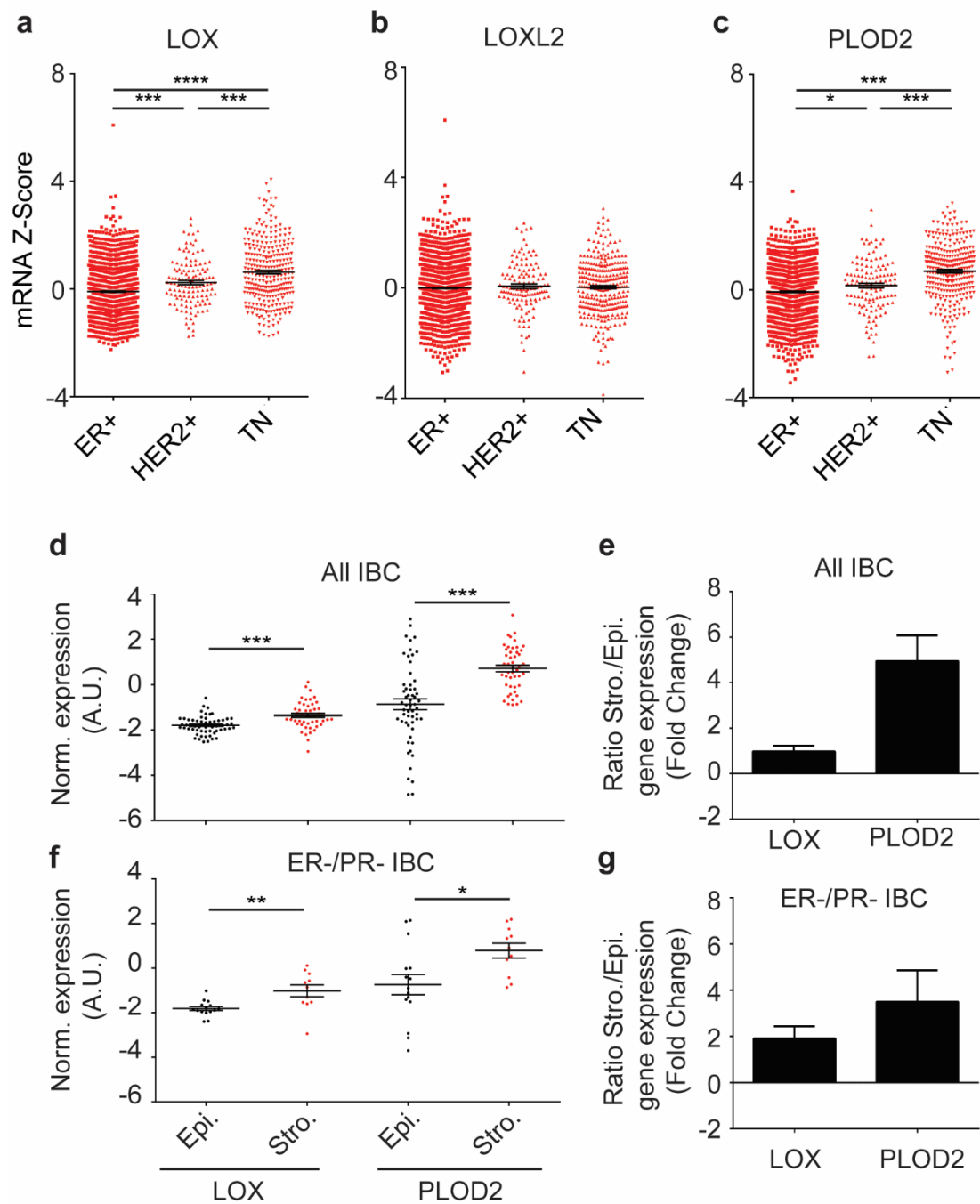
Fig 2

Figure 2: LOX and PLOD2 are enriched in TNBC and predominantly expressed by stromal cells. (**a-c**) Gene expression analysis of LOX (**a**), LOXL2 (**b**), and PLOD2 (**c**) stratified by ER$^+$ (n = 1355), HER2$^+$ (n = 127), and triple negative (TN; n = 299) subtypes. Gene expression is plotted as a scatter plot of mRNA z scores with the mean ± SEM. Statistical analysis was performed using one-way ANOVA for overall analysis and unpaired t-test was used for individual comparisons (*p < 0.05, **p < 0.01, ***p < 0.001, ****p<0.0001). (**d**) Scatter plot of individual and mean values ± SEM comparing LOX (n = 47) and PLOD2 (n = 57) gene expression in microdissected epithelial and stromal compartments of human invasive breast carcinomas. Statistical analysis was performed using Mann-Whitney U test (****p < 0.0001). (**e**) Quantification of LOX and PLOD2 gene expression fold change from (**d**) in stromal cells relative to epithelial cells. (**f-g**) Restriction of the stromal/epithelial gene expression analysis in (**d**) and (**e**) to estrogen receptor (ER) negative and progesterone receptor (PR) negative samples. (LOX n = 11, PLOD2 n = 15). Statistical analysis was performed using Mann-Whitney U test (*p < 0.05, **p < 0.01).
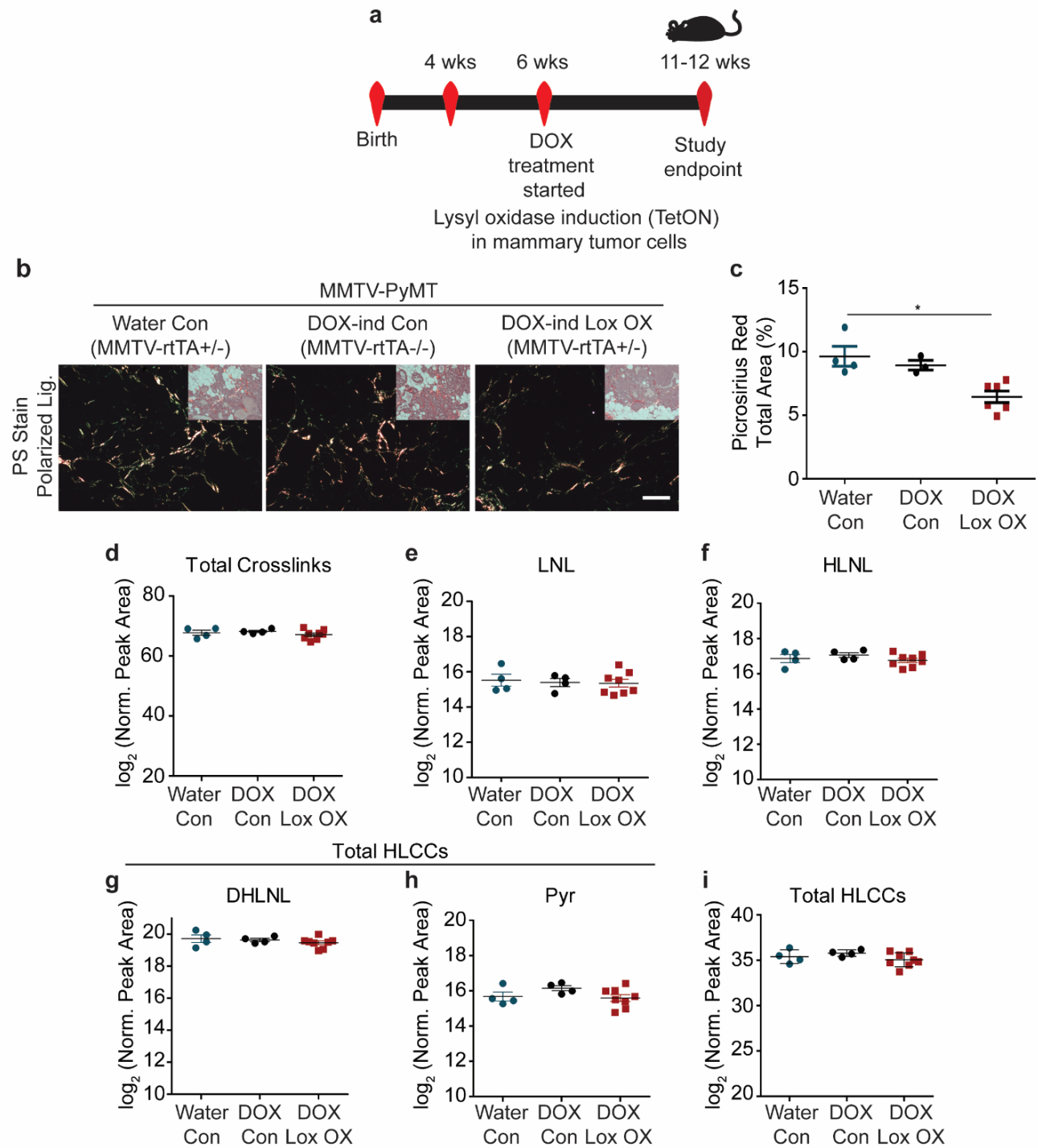
40

Fig 3

41

Figure 3: Epithelial-derived collagen crosslinking enzymes fail to induce collagen crosslinking. (**a**) Schematic depicting the experimental strategy used to induce epithelial Lox overexpression. (**b**) Polarized light images with brightfield inset of picrosirius red stained murine mammary tissues. (**c**) Quantification of percent area of picrosirius red staining per field of view, plotted as a scatter plot of the mean for each animal ± SEM. Statistical analysis was performed using Kruskal-Wallis one-way ANOVA (*p < 0.05). (**d**) Scatter plot showing individual and mean values ± SEM of total tissue collagen crosslinks in PyMT controls (Water n = 4, DOX n = 4) and PyMT epithelial Lox overexpression (n = 8). (**e-h**) Scatter plots showing individual and mean values ± SEM for each LCC and HLCC collagen crosslink measured in PyMT control and PyMT epithelial Lox overexpression tumor tissue. (**i**) Scatter plot showing individual and mean values ± SEM of total HLCCs calculated as the sum of DHLNL and Pyr crosslinks. Quantity of crosslinks per tissue was calculated normalizing crosslinks to total collagen content (i.e., hydroxyproline abundance) and wet tissue weight. Values were plotted as $\log_2$ transformed normalized peak areas as quantified from LC-MS data. Statistical analyses for crosslinking data were performed using one-way ANOVA for overall comparison and unpaired t-test for individual comparisons (*p < 0.05, **p < 0.01, ***p < 0.001, ****p < 0.0001).
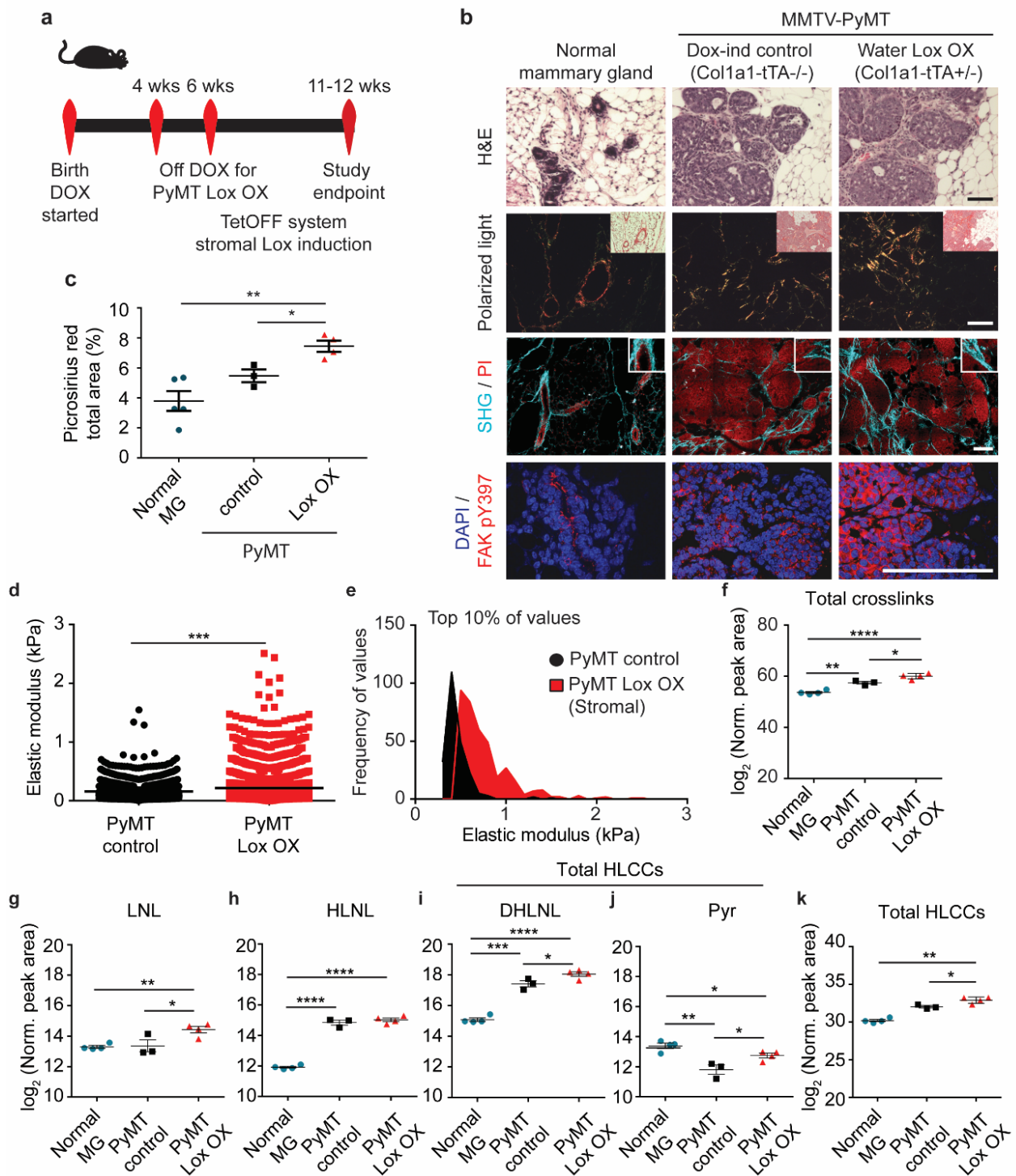
Fig 4

Figure 4: Stromal-derived LOX regulates collagen crosslinking and stiffening. (a) Schematic depicting the experimental strategy used to induce stromal Lox overexpression. (**b**) Representative images of normal murine mammary gland and PyMT control and stromal Lox overexpressing tumor tissues. (**Top row**) Brightfield images of H&E stained murine mammary tissues. (**Second row**) Polarized light images with brightfield inset of picrosirius red stained murine mammary tissues. (**Third row**) Two photon second harmonic generation (SHG) images of murine mammary tissues revealing collagen organization (turquoise) and propidium iodide (PI; red) stained nuclei. (**Bottom row**) Confocal images of mammary tissue stained with anti-FAK pY397 monoclonal antibody (red) and DAPI (blue; nuclei). Scale bars are all 100 μm. (**c**) Quantification of fibrillar collagen by picrosirius red staining by percent area per field of view. The mean of 3-5 regions was calculated and plotted for each animal ± SEM. Statistical analysis was performed using Kruskall-Wallis one-way ANOVA (*p < 0.05) for overall relationship and unpaired t-test for comparing individual groups (*p<0.05, **p<0.005). (**d**) Scatter plot showing individual values and mean of the top 10% of elastic modulus measurements performed by AFM microindentation on the mammary stroma from mice with PyMT-induced tumors (PyMT Control; n = 3 mice) as compared to the stroma in PyMT-induced tumors in which lysyl oxidase was elevated in stromal cells (PyMT Lox OX; n = 4 mice). Values reflect measurements taken from 3-5 individual force map regions per mammary gland. Statistical analyses were performed using Mann-Whitney U test (***p < 0.001). (**e**) Histogram showing the distribution of the top 10% of elastic modulus measurements by AFM microindentation in PyMT control and Lox OX tumors. Statistical analysis was performed using Mann-Whitney U test (****p < 0.0001). (**f**) Scatter plots showing individual and mean values ± SEM of total collagen crosslink abundance in the normal murine mammary gland (n = 4) as compared to glands with doxycycline-induced PyMT tumors (n = 3 mice per control group) and PyMT tumors in which stromal lysyl oxidase was elevated (n = 4 mice per Lox OX group). (**g-j**) Scatter plots showing individual and mean values ± SEM of LCC and HLCC crosslinks quantified in normal mammary gland, PyMT Control tumors and PyMT Lox OX tumors. (**k**) Scatter plot showing individual and mean values ± SEM of total HLCCs calculated as the sum of DHLNL and Pyr crosslinks. Quantity of crosslinks per tissue was calculated normalizing crosslinks to total collagen content (i.e., hydroxyproline abundance) and wet tissue weight. Values were plotted as $\log_2$ transformed normalized peak areas as quantified from LC-MS data. Statistical analyses for crosslinking data were performed using one-way ANOVA for overall comparison and unpaired t-test for individual comparisons (*p < 0.05, **p < 0.01, ***p < 0.001, ****p < 0.0001).
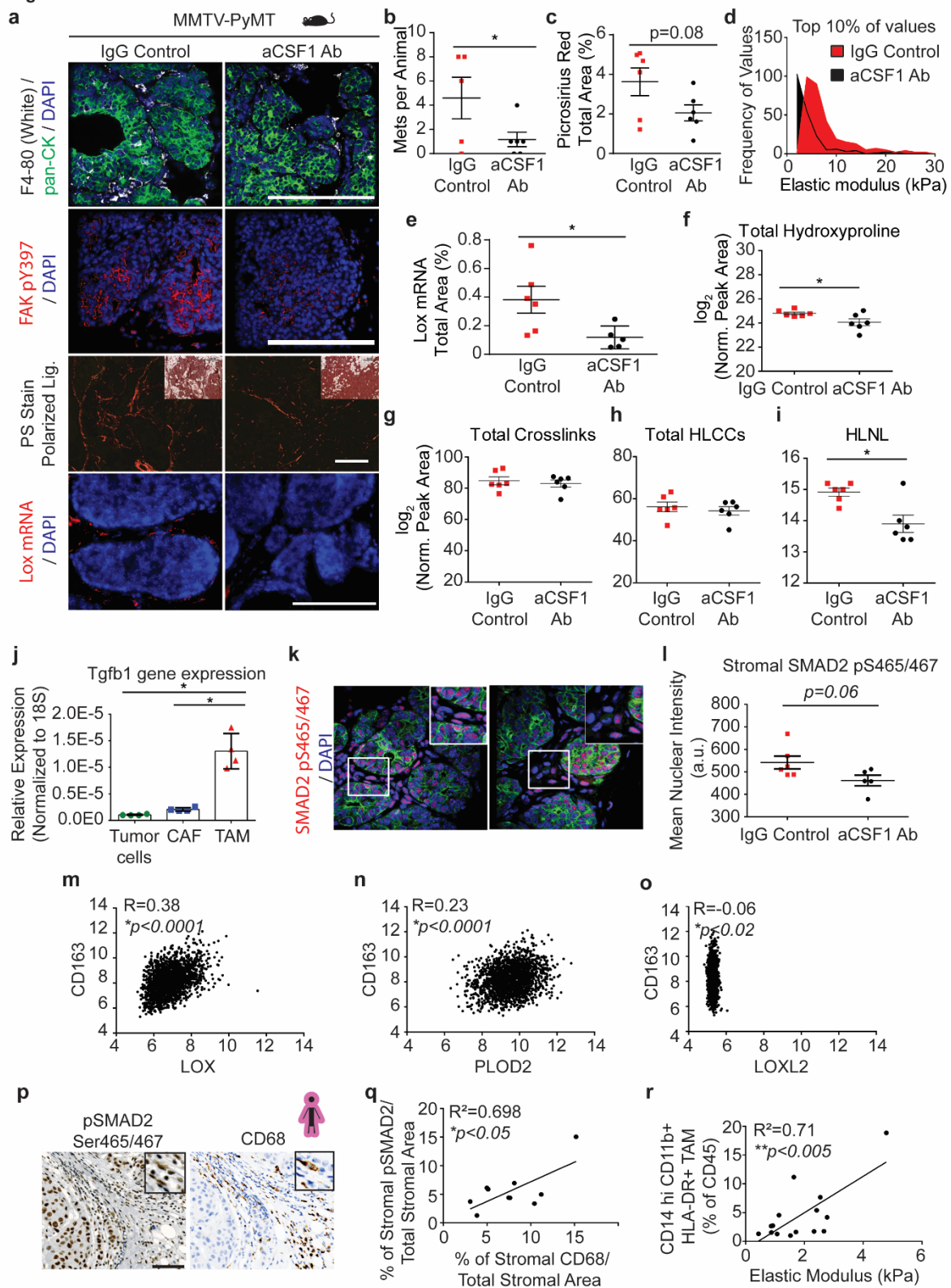
Fig 5

Figure 5: Tumor infiltrating macrophages secrete TGFb to activate stromal-mediated collagen crosslinking. (**a**) Representative images of PyMT tumor tissue from 8 weeks of age mice treated with anti-CSF1 blocking antibody or IgG1 control. (**Top row**) IgG1 treated (n = 6) and anti-CSF1 treated (n = 5) PyMT tumor tissue stained for pan-cytokeratin (green) marking epithelial cells, F4/80 (white) marking tumor infiltrating macrophages, and DAPI marking nuclei (blue). (**Second row**) IgG1 treated (n = 6) and anti-CSF1 treated (n = 5) PyMT tumor tissue stained for tyrosine 397 phosphorylated focal adhesion kinase (red) indicative of mechanosignaling and DAPI marking nuclei (blue). (**Third row**) Polarized light images with brightfield inset of IgG1 treated (n = 6) and anti-CSF1 treated (n = 6) PyMT tumor tissue stained with picrosirius red to visualize fibrillar collagen. (**Bottom row**) Lox mRNA in situ hybridization in IgG1 treated (n = 6) and anti-CSF1 treated (n = 5) PyMT tumor tissue and DAPI marking nuclei (blue). Scale bar for all images is 100µm. (**b**) Quantification of the number of metastatic colonies in the lung tissues from IgG1 treated (n = 5) and anti-CSF1 treated (n = 6) mice at 11 weeks of age via PyMT IHC assessing 5 layers (5 micron section; 5 sections per layer; 50-100 microns steps). Statistical analysis was performed using unpaired t-test (*p < 0.05). (**c**) Quantification of fibrillar collagen by picrosirius red staining by percent area per field of view in 8 week old mice treated with anti-CSF1 blocking antibody or IgG1 control. The mean of 3-4 regions was calculated and plotted for each animal ± SEM. Statistical analysis was performed using unpaired t-test (p = 0.08). (**d**) Histogram showing the distribution of the top 10% of elastic modulus measurements by AFM microindentation in PyMT IgG1 treated (n =6) and anti-CSF1 treated (n = 4) tumors. Statistical analysis was performed using Mann-Whitney U test (****p < 0.0001). (**e**) Quantification of Lox mRNA signal by percent area of signal per field of view in 8 week old mice treated with anti-CSF1 blocking antibody (n = 5) or IgG1 control (n = 6). The mean of 5-6 regions was calculated and plotted for each animal ± SEM. Statistical analysis was performed using an unpaired t-test (*p < 0.05). (**f-i**) Scatter plots showing individual and mean values ± SEM of the levels of total hydroxyproline (collagen content) (**f**), total collagen crosslinks (**g**), HLCCs (**h**), and HLNL crosslinks (**i**) in 8 week old IgG1 treated and anti-CSF1 treated PyMT tumors. Quantity of crosslinks per tissue was calculated normalizing crosslinks to wet tissue weight. Values were plotted as log_2 transformed normalized peak areas as quantified from LC-MS data. Statistical analysis was performed using unpaired t-test (*p < 0.05). (**j**) Quantification of Tgfb1 gene expression by RT-qPCR in tumor cells, cancer-associated fibroblasts, and macrophages sorted out from PyMT tumors (n = 4). Gene expression was normalized to 18S. Statistical analysis was performed using Kruskal-Wallis one-way ANOVA for overall comparison and Mann-Whitney U test for individual comparisons (*p < 0.05, ***p < 0.001). (**k**) Representative images of PyMT tumor tissue from mice treated with IgG1 (n = 6) and anti-CSF1 (n = 5) stained for pan-cytokeratin (green) marking epithelial cells, SMAD2 pS465/467 (red), and DAPI marking nuclei (blue). (**l**) Scatter plot showing individual and mean values ± SEM of the mean nuclear intensity of pSMAD[S465/467] in stromal cells of IgG1 treated (n = 6) and anti-CSF1 treated (n = 5) PyMT mice. The mean for each animal was calculated from 4-7 regions within the tumor. Statistical analysis was performed using unpaired t-test (p = 0.06). (**m-o**) Scatter plot depicting the Spearman correlation of CD163 gene expression with LOX (**m**), PLOD2 (**n**), and LOXL2 (**o**) in human breast tumors (n = 1904). (**p**) Representative IHC images of serial human breast tumor sections stained for CD68 (**top**) and pSMAD2[S465/467] (**bottom**) counterstained with hematoxylin to mark nuclei. (**q**) Scatter plot depicting the linear regression correlation of stromal pSMAD2 IHC staining with stromal CD68 IHC staining in human breast tumors (n = 10). (**r**) Scatter plot depicting the linear regression of CD14^{+} CD11b^{+} HLA-DR^{+} tumor associated macrophage infiltrate with tumor elastic modulus as measured by AFM microindentation in human breast tumors (n = 15).
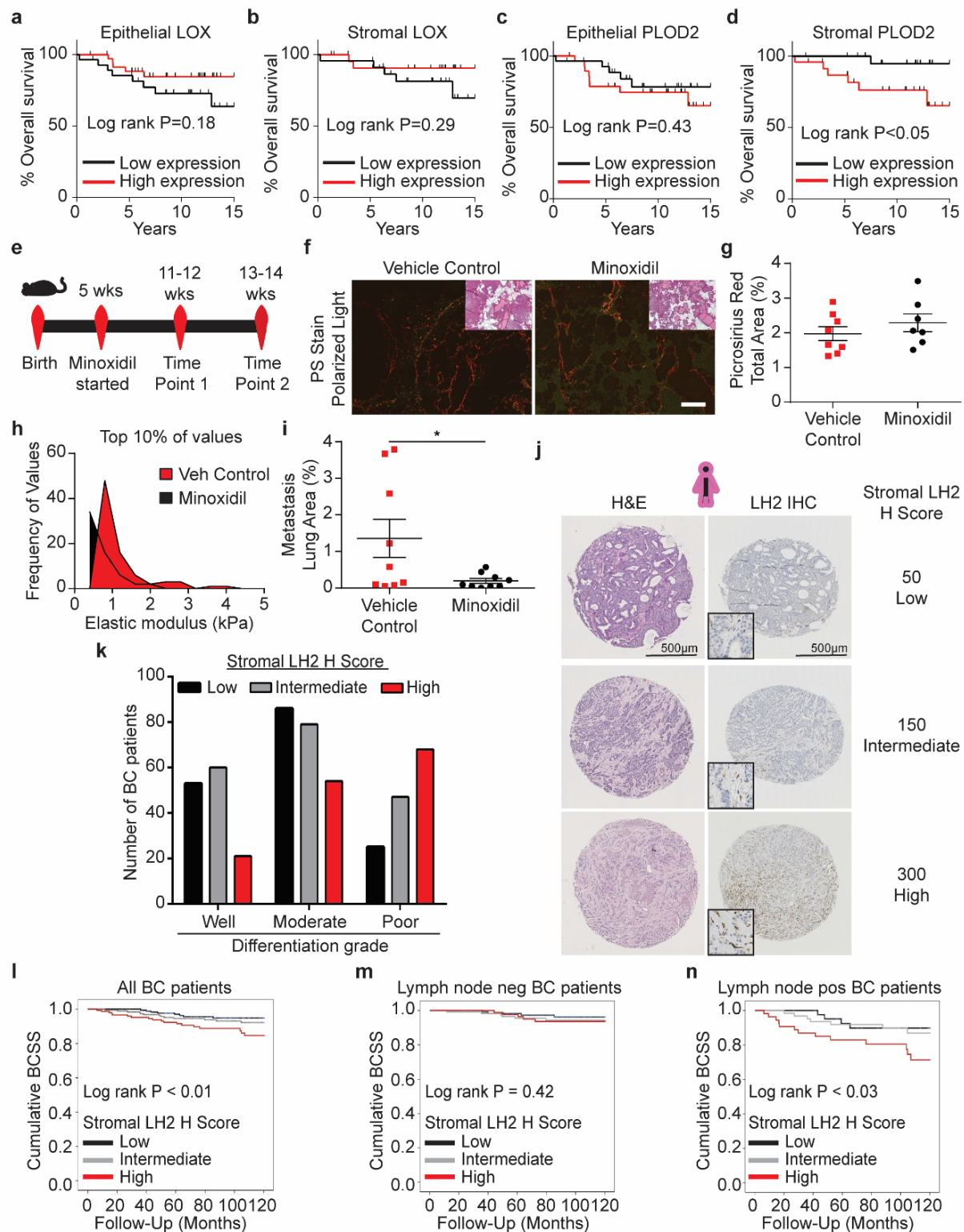
Fig 6

Figure 6: Stromal LH2 predicts poor patient outcomes. (**a-b**) Kaplan-Meier plots showing overall survival for patients based on levels of LOX expression in epithelial cells (low n = 28, high n = 36) (**a**) or stromal cells (low n = 23, high n = 24) (**b**). The median level of expression was defined as the cutoff for low and high expression. (**c-d**) Kaplan-Meier plots showing overall survival for patients based on levels PLOD2 expression in epithelial cells (low n = 28, high n = 29) (**c**) or stromal cells (low n = 23, high n = 24) (**d**). The median level of expression was defined as the cutoff for low and high expression. (**e**) Schematic depicting the experimental timeline used to inhibit lysyl hydroxylase 2 in PyMT mice. (**f**) Representative polarized light images with brightfield insets of picrosirius red stained tumor tissue from PBS vehicle treated control (n = 8) and minoxidil treated (n = 7) PyMT mice. Scale bar is 100um. (**g**) Quantification of fibrillar collagen by picrosirius red staining by percent area per field of view. The mean was calculated and plotted for each animal ± SEM. (**h**) Histogram showing the distribution of the top 10% of elastic modulus measurements by AFM microindentation in PyMT control and Lox OX tumors. Statistical analysis was performed using Mann-Whitney U test (****$p < 0.0001$). (**i**) Scatter plot quantifying the area of lung sections occupied by metastases from vehicle treated (n = 9) and minoxidil treated (n = 8) mice at 13 weeks of age via H&E staining and assessing 4 layers (5 micron section; 5 sections per layer; 50-100 microns steps). Statistical analysis was performed using a two-tailed unpaired t-test (*$p < 0.05$). (**j**) Representative phase contrast images of sections from tissue microarrays (TMAs) of human breast cancers representing incident breast cancer cases collected and arrayed as 1-mm cores from each tumor. Sections were stained with Hematoxylin and Eosin (H&E; top) and lysyl hydroxylase two (LH2; bottom) via immunohistochemistry. (**k**) Bar graphs showing clinical correlation between lysyl hydroxylase two (LH2) score as a function of tumor grade (*see Table 1 for number of patients*). LH2 IHC staining was assessed with the semi-quantitative stromal specific H-score from 0 to 300. The lowest tertile of LH2 H-scores was defined as H-scores between 0 and less or equal to 120, the intermediate H-score to above 120 and equal or less than 230, and the highest stromal LH2 score as above 230. For tumor grade and LH2 H score, statistical analysis was performed using a linear-by-linear association (***$P<0.0001$). (**l**) Kaplan-Meier curves indicating cumulative breast cancer specific survival (BCSS) based on stromal LH2 H score assessed in breast cancer patients up to 10 years after diagnosis (LH2 low n = 175, intermediate n = 188, high n = 146). (**m**) BCSS curves by stromal LH2 H score including only axillary lymph node negative patients (LH2 low n = 116, intermediate n = 116, high n = 90). (**n**) BCSS curves by stromal LH2 H score including only axillary lymph node positive patients (LH2 low n = 44, intermediate n =63, high n = 54). For Kaplan-Meier curves, statistical analyses were performed by LogRank test.